High Dimensional Planning and Learning for Off-Road Driving

Guan-Horng Liu

CMU-RI-TR-17-37

June 2017

The Robotics Institute
Carnegie Mellon University
Pittsburgh, PA 15213

Thesis Committee:
George Kantor, Chair
Sebastian Scherer
Devin Schwab

Submitted in partial fulfillment of the requirements for the degree of Masters of Science in Robotics.

For the mysteries of the universe that I am so addicted to.

Abstract

This thesis explores both traditional motion planning and end-to-end learning algorithms in the off-road settings. We summarize the main contributions as 1) propose an RRT-based local planner for high-speed maneuvering, 2) derive a novel stochastic regularization technique that robustifies end-to-end learning in the spirit of sensor fusion, and 3) traversability analysis of the unstructured terrain using deep inverse reinforcement learning (DIRL) algorithms. We first propose a sample-based local planner that is modified to solve a minimal traveling-time trajectory problem subjected to a data-driven vehicle model in high dimensional state space. The planner is implemented on a full-size All-Terrain Vehicle (ATV), and the experimental results show that it can successfully avoid obstacles on a turnpike with the vehicle velocity up to the maximum operating speed. Secondly, we also propose a stochastic regularization technique, called *Sensor Dropout*, that promotes an effective fusing of information for end-to-end multimodal sensor policies. Through empirical testing on a physical-based racing car simulator called *TORCS*, we demonstrate that our proposed policies can operate with minimal performance drop in noisy environments, and remain functional even in the face of a sensor subset failure. Lastly, we investigate into the DIRL algorithms that infer the traversability of the unstructured terrain by leveraging a large volume of human demonstration data collected on the field. We propose several modifications to overcome issues that arise from DIRL training, such as sparse gradients and ambiguity of the demonstration optimality. The framework is tested on the full-size ATV.

Acknowledgments

First, I would like to thank my advisor, Mr. George Kantor, for providing me advice, financial supports, and most importantly introducing me to the Yamaha ATV project that provides me a great opportunity to implement and test algorithms on the full-size autonomous vehicle.

I would also like to thank all of the members in the Yamaha ATV project, especially Jay Hiramatsu who supports most of the field experiments I need to finish this thesis. I appreciate every valuable discussion with many intelligent students here: Po-Wei, Wei-Hsin, Daniel, Sai. Discussions with senior Ph.D. students: Avinash Siravuru, Ming Hsiao, Humphrey Hu, Yen-Chia Hsu, and Devin Schwab inspire me frequently. I have big special thanks to Po-Wei Chou, both my project-mate and roommate, with whom I enjoy sharing my point of views and discuss. I would not make through my first year here without your help and collaborations. I would also like to thank Ming Hsiao for helping me polish the speaking qualifier.

Lastly, I would like to thank my parents for providing me sufficient resources and accesses to education in my life, and supporting most of my career decisions. I believe I owe so much to Bonnie Chen, for supporting me over the two years of long distance during the master program. I would not make all those tough times through without you beside me.

Contents

1 Introduction **1**
- 1.1 Motivation . . . 1
  - 1.1.1 Traditional Motion Planner . . . 2
  - 1.1.2 Learning End-to-end Controller . . . 2
- 1.2 Approaches . . . 4

2 Related Work **7**
- 2.1 Sample-Based Planning . . . 7
- 2.2 Deep Reinforcement Learning (DRL) . . . 8
  - 2.2.1 Continuous Action Space Algorithms . . . 9
- 2.3 Stochastic regularization . . . 11
- 2.4 Deep Inverse Reinforcement Learning (DIRL) . . . 11

3 Model Predictive Planning **15**
- 3.1 Vehicle Response Model . . . 15
- 3.2 Planner Design . . . 17
  - 3.2.1 Collision Check Module . . . 17
  - 3.2.2 Sample-based Planner Module . . . 19
- 3.3 Experiments and Analysis . . . 21
  - 3.3.1 Vehicle Model Verification . . . 22
  - 3.3.2 Planner Demo . . . 22

4 Learning End-to-end Multimodal Sensor Policy **25**
- 4.1 Proposed Methods . . . 26
  - 4.1.1 Multimodal Network Architecture . . . 26
  - 4.1.2 Sensor-based Dropout (SD) . . . 26
  - 4.1.3 Augmenting Auxiliary Loss . . . 28
- 4.2 Evaluation and Analysis . . . 28
  - 4.2.1 Platform Setup . . . 28
  - 4.2.2 Experimental Results . . . 30
- 4.3 Discussion . . . 34
  - 4.3.1 Full Sub-Policy Analysis . . . 34
  - 4.3.2 Visualize Policy Attention Region . . . 35
- 4.4 Supplementary Material . . . 36

5 Learning from Demonstration using DIRL **37**
5.1 Proposed Methods 37
5.1.1 Learning from Failure for DIRL 37
5.1.2 Modeling Optimality Ambiguity 38
5.2 Experiments Results 39

6 Conclusion and Future Work **43**

Bibliography **45**

List of Figures

1.1 Some well-known autonomous navigation systems: (a) The Carnegie Mellon Tartan that won the Urban Challenge in 2007 [1]. (b) Uber's self-driving vehicle. (c) Crusher. [2] 1

1.2 Demonstrations of the end-to-end approach on autonomous navigation applied to (a) the realistic simulator (GTA V), and (b) the full-size vehicle by NVIDIA[3]. 3

1.3 Recent successes on applying deep reinforcement learning (DRL) algorithms to real-world robotics problems: (a) manipulation [4]. (b) autonomous navigation. [5] 3

2.1 Schematic illustration of (a) forward and (b) back-propagation for NAF, and (c) forward and (d) back-propagation for DDPG. Green modules are functions approximated with deep nets. 10

2.2 The block diagram of reinforcement learning and inverse reinforcement learning. 11

2.3 Schematic illustration of deep inverse reinforcement learning. 12

3.1 (a) Notation of vehicle velocity in local frame. (b) Data flow of conventional dynamic response model. The model takes two velocity control commands as input and estimates the velocity response in vehicle frame. (c) Schematic illustration of neural network based response model from [6]. 16

3.2 Block Diagram of our planner API. 17

3.3 Three different methods of collision check. Note that for (b), the original and the processed point cloud is represented by white and colored dot, respectively. . . . 18

3.4 Simulation of RRT planner with vehicle model derived in Sec. 3.1 19

3.5 The visualization of RRT-based planner. 20

3.6 The testing vehicle platform and the onboard sensor. 22

3.7 Simulated velocity response w.r.t. time steps. Note that the blue line is measured under an accurate GPS/INS sensor with RTK signal. We refer this measurement as our ground true data. 23

3.8 Comparison between data-driven dynamic model and original kinematic model. Note the time interval in each graph is 20 seconds. 24

3.9 Screenshots of planner visualization output. The green path is the trajectory where each point is encoded with a 6 DoF state, 2 DoF control input, and a control duration. The red points are the filtered point cloud segmented as obstacles. 24

4.1 Illustration of multimodal sensor policy network augmented with Sensor Dropout. The operation $*$ stands for element-wised multiplication. The dropping configuration of Sensor Dropout is sampled from a categorical distribution, which the network takes as an additional input. The feature extraction module can be either pure identity function (modality 1), or convolution-based layer (modality $2 \rightarrow M$). The operation $\odot *$ stands for element-wised multiplication. 27
4.2 Sensors used in the TORCS racing car simulator: *Sensor 1:* Physical information such as velocity (a), position, and orientation (b), *Sensor 2:* Laser range finder (c), and *Sensor 3:* Front-view camera (d). 29
4.3 Training performance comparison of three baseline single sensor policies, and the proposed multimodal sensor policies, with and without Sensor Dropout. . . . 30
4.4 Policy Robustness Analysis: Darker lines connects average rewards of leaned policies with accurate sensing while the lighter lines connects the corresponding policies in the face of sensor noise. 31
4.5 Policy Robustness Analysis: The bar box measures the relative scale among each of the models when noise is introduced. The red dotted lines show the performance without noise. 31
4.6 Policy performance when facing random sensor failure. 32
4.7 Two-dimensional PCA embedding of the representations in the last hidden layer assigned by the policy networks. 33
4.8 The variance of all the actions induced by sub-policy under each multimodal sensor policy. *Upper-left*: naive policy without any regularization. *Upper-right*: with standard Dropout. *Lower-left*: with Sensor Dropout. *Lower-right*: with Sensor Dropout and auxiliary loss. 34
4.9 The full analysis of the performance of the total 6 sub-policies. The (1), (2), and (3) labels in y-axis represent physical state, laser, and image, respectively. The x-axis represents the remaining performance w.r.t. the SD policy with all sensor, *i.e.* (1)+(2)+(3). 35
4.10 (a)The visualization of the magnitude of gradient for each neuron. The whiter color means the higher gradient. The color bar represents three different sensor modules: physical state(blue), Laser(green), and Image(red). (b) The gradient responses of actions on the image input for each of the multimodal agents. The top 20% gradients are marked red. 35

5.1 Block diagram of deep inverse reinforcement learning. 38
5.2 The extracted feature maps from LiDAR. The flow chart is shown on the left of the figure, while examples of the actual collected data on field are shown on the right of the figure. 39
5.3 Training curve of DIRL in Gascola dataset. 39
5.4 Final cost map on testing set. The left, middle, and right image represent the output cost map, the same cost map overlapped with expected SVF, and with demonstrations, respectively. 40
5.5 Samples of intermediate cost maps during training. 41

List of Tables

3.1 Simulation Benchmark 19
3.2 Planner Hyper-parameter 21

4.1 Model Specification 30
4.2 Performance of Policy 32
4.3 Results of the sensitivity metric. 32
4.4 Covariance of the first three Principal Component 36
4.5 Action Variation w.r.t. multimodal sensor 36

Chapter 1

Introduction

1.1 Motivation

In modern autonomous systems, *motion planning* refers to a process where the desired movement task is broken into discrete motions that satisfy movement constraints and possibly optimize some aspect of the movement [7]. For autonomous navigation system, the motion planning algorithm gathers information from sensors, performs optimization over the cost of the trajectory toward the desired configuration state (subjected to vehicle constraints if needed), and finally outputs the action commands for execution. It is worth noting that for complex decision making tasks, raw sensor information is usually processed through additional *perception* module to extract informative features before entering the motion planning module. In this viewpoint, the motion planning module stands in a crucial position throughout the decision-making pipeline in that the potential imperfect sensings, resulted from sensor noise and erroneous inferences of the perception module, are accumulated here. Furthermore, accurate yet efficient decisions need to be made with minimal computations.

Recently, great strides have been made in the development of autonomous driving technologies, energized by the successful demonstrations by some teams at the DARPA Urban Challenge [1, 8]. While there is a foreseeable trend on operating autonomous driving technologies on-road within a decade, researchers have gained interests in solving extreme/aggressive motion planning in the off-road situations or unstructured terrain [9, 10, 11, 12, 13, 14]. This thesis

Figure 1.1: Some well-known autonomous navigation systems: (a) The Carnegie Mellon Tartan that won the Urban Challenge in 2007 [1]. (b) Uber's self-driving vehicle. (c) Crusher. [2]

investigates both traditional motion planning and alternative end-to-end learning algorithms in the off-road settings. Specifically, we are interested in planning and learning approaches for unmanned ground vehicles in high-dimensional state space, which arise inevitably in traditional model-based planning approaches when using a more complex vehicle model, or in end-to-end learning algorithms that directly use raw sensor streams as its inputs.

1.1.1 Traditional Motion Planner

The two most common approaches for ground vehicles motion planning are the graph-based planner and sample-based planner. Both approaches have shown their robustnesses in the DARPA Urban Challenge [15, 16] and UPI program [2, 17], where the feasible trajectories can be solved efficiently under certain reasonable assumptions. The output trajectories can be fine-tuned with optimization techniques to ensure criteria such as smoothness and kinematic constraints [18].

Though graph-based planning research has advanced significantly in recent years for the application of off-road navigation [2, 17], it is limited to the low-dimensional configuration space. For problems that require much more complicated modeling of the dynamic systems, such as maneuvering agilely and aggressively on rough terrain, it will inevitably lead to a higher dimensional configuration space, and thus slows down the standard graph-based approaches. In fact, one of the main challenges for off-road motion planning comes from the fact that the vehicle dynamics are much more unpredictable in contrast to on-road conditions. Factors such as wheel-terrain interaction for modeling the sliding effect is still an active research area [19, 20].

Sample-based planners, on the other hand, are more efficient in solving higher-dimensional motion planning. Built upon the successful application of randomized approaches to many robotics problems such as manipulation [21], researchers have tried to extend the approaches to provide aggressive motion planning for vehicles that exhibit dynamics behaviors such as drifting [22]. However, unlike graph-based planners that guarantee a certain level of optimality, sample-based planners in general only permit asymptotic convergence to the optimal solution. Moreover, it is not straight-forward to implement in kinodynamic planning problems.

Despite the pros and cons of each approach, they both share a common framework where an intelligent pipeline is built to efficiently gather incoming sensor data and take suitable control actions with good repeatability and fault-tolerance. The resulting autonomous navigation system is addressed in a modular fashion, where specialized algorithms are developed for each subsystem and finally integrated with some fine tunings.

1.1.2 Learning End-to-end Controller

More recently, however, there is an interest in applying an end-to-end approach wherein one can learn a complex mapping that goes directly from the input (e.g., camera images or laser scan measurements) to the output (e.g., steering and throttle commands) by leveraging the availability to a large volume of task-specific data. The end-to-end approaches have become more appealing with the use of deep learning in robotics and have shown successes in developing visuomotor policies for autonomous driving [3, 23, 24]. However, the traditional deep supervised learning-based driving requires a great deal of human annotation and may not be able to deal with the problem of accumulating errors [25].

Figure 1.2: Demonstrations of the end-to-end approach on autonomous navigation applied to (a) the realistic simulator (GTA V), and (b) the full-size vehicle by NVIDIA[3].

On the other hand, deep reinforcement learning (DRL) offers a better formulation that allows policy improvement with feedback, and has achieved human-level performance on several video games [26, 27, 28]. The choice of DRL over the more tried and tested waters of supervised learning comes from the interest of better generalization and allowing for a more exploration-friendly setting. Recently, there have been great demands and improvements on realistic simulators [29, 30] with the hope that the acquired learning in such a simulator can be transferable to the real world with minimal tuning [31].

Previous work in DRL predominantly learned policies based on a single input modality, *i.e.*, either low-dimensional physical states or high-dimensional pixels. For autonomous driving where enhancing safety and accuracy to the maximum possible extent is a top priority, developing policies that operate with multiple inputs is the need of the hour. In this light, several recent works in DRL have tried to solve the complex robotics tasks such as human-robot-interaction [32], manipulation [33], and maze navigation [34] with multi-sensor inputs. It is worth mentioning that though Mirowski et al. [34] uses multi-sensor inputs to navigate through a maze, information such as depth is only used as an auxiliary loss, *i.e.* it is not an input to the trained policy but is only used to improve the learning outcomes. In fact, Mirowski et al. [34] points out that the naive RGBD policy performs worse than predicting depth as a regression task.

Our observation is that though these end-to-end learning approaches have a great potential to handle high-dimensional state space, in the multi-sensor setting the learned policy may either become over-dependent on partial sensor subset or rely heavily on all the inputs to the extent that it fails completely if a single sensor becomes unreliable. To be clear, in the space of end-to-end sensorimotor control, the *sensor fusion* outlook, as an indispensable technique to improve accu-

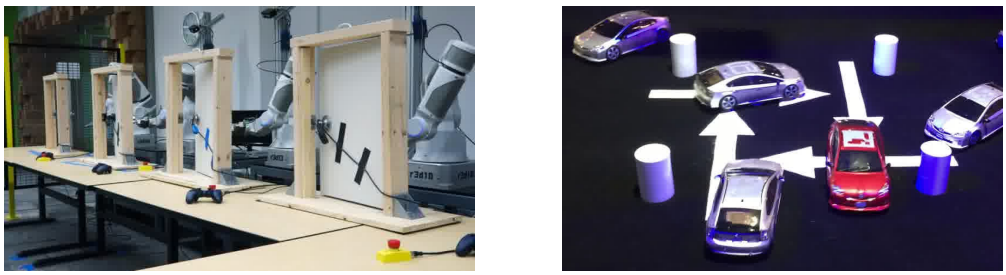

Figure 1.3: Recent successes on applying deep reinforcement learning (DRL) algorithms to real-world robotics problems: (a) manipulation [4]. (b) autonomous navigation. [5]

racy and robustness in a modern autonomous navigation system, has received limited attention. In fact, multimodal perception is an integral part of autonomous navigation solutions and even played a critical role in their success [8] before the advent of end-to-end deep learning based approaches. It offers several advantages, namely robustness to individual sensor noise/failure, improved object classification and tracking [35, 36, 37], robustness to varying weather and environmental conditions, etc. This problem is critical as a further step toward the real-world robotics application given the current state-of-the-art DRL agents on many realistic simulators.

1.2 Approaches

In this thesis, we first propose a model-based local planner that solve the optimal kinodynamic motion planning problem. The local planner is built upon a vehicle model that captures important state for off-road navigation such as lateral velocity. Practical problems such as re-planning and optimization are addressed under the standard sample-based approach but modified appropriately to encourage a more aggressive maneuvering. The resulting model-predictive planner is tested on the full-size All-Terrain Vehicle (ATV) in the off-road conditions.

We also present an alternative end-to-end controller that uses multi-sensor input to learn an autonomous navigation policy in a physics-based gaming environment called TORCS [38]. To show the effectiveness of multimodal perception, we pick two popular continuous action DRL algorithms, namely Normalized Advantage Function (NAF) [39] and Deep Deterministic Policy Gradient (DDPG) [40], and augment them to accept multimodal inputs. Though a multimodal sensor policy may improve the reward of the agent, it provides no guarantees on the sensitivity of the trained policy to each sensor module. This undesirable consequence renders sensor redundancy useless. To ensure that the learned policy does not succumb to such over-fitting, we apply a novel stochastic regularization method called *Sensor Dropout* during training. Our approach reduces the policy sensitivity to a particular sensor subset and makes it capable of functioning even in the face of partial sensor failure. Based on the Sensor Dropout, we further embedded the standard DRL loss with an auxiliary loss that helps reduce the action variations of the multimodal policy.

Note that both the traditional and the end-to-end planner require the cost/reward heuristic function to guide the policy and formally define the optimization problem. However, unlike in the urban environment where cost function can be well defined in a rule-based structure, finding a cost function for off-road navigation can be non-trivial and often requires lots of handy tunings [41]. Here, motivated by the recent successes [42, 43], we also investigate into the using deep neural network as a function approximator to construct the cost/reward function under deep inverse reinforcement learning (DIRL) platform. Again, we can leverage the availability to a large volume of task-specific data and solve the problem with minimal engineering hand-tunings.

To summarize, the primary contributions of this thesis are:

1. Propose a model-based local planner for high-speed maneuvering in the off-road navigation application. The planner uses Rapidly-exploring Random Tree (RRT) [21] as its template, and is tested on a full-size all-terrain vehicle (ATV) in the off-road environment. We show that the planner can perform smooth yet aggressive avoid static obstacles with high speed up to $30kph$.

2. Propose a new stochastic regularization, namely *Sensor Dropout*, for training an end-to-end multi-sensor policy under deep reinforcement learning (DRL) framework. The proposed method is integrated with two continuous action algorithms and heavily tested on a physics-based gaming environment called TORCS [38]. We show that policies trained with Sensor Dropout not only perform minimal performance drop when measurements become noisy/imperfect, but are also less sensitive to any single sensing modality; therefore, makes it able to function even in the face of partial sensor failure.
3. Investigate into the deep inverse reinforcement learning (DIRL) algorithms that infer the cost, or traversability, of the unstructured terrain by leveraging large volume of human demonstration data collected on the field. We propose two slight modifications over the current approach [42], including explicitly modeling the ambiguity of optimality, and integrating with failure demonstrations to overcome the spatially sparse gradient in DIRL training. The framework is tested on a full-size ATV in the off-road environment.

The thesis is organized as follows: In Chapter 2 we briefly go through the preliminary background, including the basic sample-based planner, the formal definition of deep (inverse) reinforcement learning, related stochastic regularization in the multimodal learning literature, and the two continuous action agents used in this work. In Chapter 3 we formulate our model predictive planner, followed with the derivation of the vehicle model, detailed planner design for optimal planning, and finally the experimental results on the field. In Chapter 4 we propose a new technique at the aspect of sensor fusion to improve the performance of the end-to-end controller with multi-sensor inputs. In Chapter 5 we investigate the traversability analysis with the recently popular studies on deep inverse reinforcement learning. Finally, we conclude the work in Chapter 6 and address some of the interesting directions for future works.

Chapter 2

Related Work

2.1 Sample-Based Planning

Sample-based planners search for the feasible paths through the configuration space in a probabilistic fashion. Similar to graph-based approaches, the validity of configuration space need not be explicitly formulated; instead, we only need a function that determines whether a specific configuration is valid. The probabilistic property makes sample-based planners suitable to tackle high dimensional configuration space planning problems, yet with the trade-off on the sub-optimality of the solution. The Rapidly-exploring Random Tree (RRT) is a sampling-based planner which build trees of valid trajectories (edges) between points in configuration space (nodes). As shown in Algorithm 1 [44], to grow these graphs, a new point in configuration space is sampled, and the closest point on the existing tree is extended towards this sampled point.

Algorithm 1 RRT

1: $T \leftarrow$ InitTree(x_{start})
2: **while** GoalNotReached(T, X_{goal}) **do**
3: $x_{sample} \in X \leftarrow$ Sample()
4: $x_{nearest} \leftarrow$ Nearest(T, x_{sample})
5: $x_{new} \leftarrow$ Extend($x_{nearest}, x_{sample}$)
6: T $\leftarrow$UpdateTree($(x_{nearest}, x_{new}), T$))
7: **end while**

The Extend function constructs a linearly trajectory in the configuration space from $x_{nearest}$ towards x_{sample}. The extension terminates at x_{new} either when x_{sample} is reached, or when the trajectory enters an invalid region, which can be specified by the validity function mentioned in the previous paragraph, or a hyper-parameter *step size*. However, the standard RRT planner does not guarantee optimality of the solution.

Karaman and Frazzoli [45] proposes an extended version of RRT that follows an asymptotic convergence to the optimal solution. As shown in Algorithm 2, the new algorithm, named RRT*, preserves the original structure yet embeds the following two additional procedures.

1. Instead of extending the tree from $x_{nearest}$ towards x_{new}, we search on a subset X_{near} centered at $x_{nearest}$ to find an alternative candidate. The new node x_{min} should be collision free

and follows the constraint: $cost(x_{start}, x_{min}) + cost(x_{min}, x_{new}) < cost(x_{start}, x_{nearest}) + cost(x_{nearest}, x_{new})$.

2. Replace the original edges from x_{min} to $x_{nearest}$ with $E(x_{min}, xnew)$ and $E(x_{new}, x_{nearest})$ if the resulting trajectory has lesser cost.

Algorithm 2 New Extend and Update Function in RRT*

$x_{new} \leftarrow$ Extend($x_{nearest}, x_{sample}$)
$X_{min} \leftarrow$ LocalSearch(T, x_{new})
$x_{min} \leftarrow x_{nearest}$
for each $x \in X_{min}$ **do**
    $oldCost \leftarrow cost(x_{start}, x_{nearest}) + cost(x_{nearest}, x_{new})$
    $newCost \leftarrow cost(x_{start}, x) + cost(x, x_{new})$
    if $newCost < oldCost$ **then**
        $x_{min} \leftarrow x$
    end if
end for
T $\leftarrow$ UpdateTree($(x_{min}, x_{new}), T$))
for each $x \in X_{min}$ **do**
    $oldCost \leftarrow cost(x, x_{nearest})$
    $newCost \leftarrow cost(x_{new}, x_{nearest})$
    if $newCost < oldCost$ **then**
        $E \leftarrow E \setminus (x, x_{nearest})$
        $E \leftarrow E \cup (x_{new}, x_{nearest})$
    end if
end for

2.2 Deep Reinforcement Learning (DRL)

We consider a standard Reinforcement Learning (RL) setup, where an agent operates in an environment E. At each discrete time step t, the agent observes a state $s_t \in \mathcal{S}$, picks an action $a_t \in \mathcal{A}$, and receives a scalar reward $r(s_t, a_t) \in \mathbb{R}$ from the environment. The return $R_t = \sum_{i=t}^{T} \gamma^{(i-t)} r(s_i, a_i)$ is defined as total discounted future reward at time step t, with γ being a discount factor $\in [0, 1]$. The objective of the agent is to learn a policy that eventually maximizes the expected return, as shown below:

$$J = \mathbb{E}_{s_i, r_i \sim E\ , a_i \sim \pi}[R_1] \tag{2.1}$$

The learned policy, π, can be formulated as either stochastic $\pi(a|s) = \mathbb{P}(a|s)$, or deterministic $a = \mu(s)$. The value function V^{π} and action-value function Q^{π} describe the expected return for each state and state-action pair upon following a policy π.

$$V^{\pi}(s_t) = \mathbb{E}_{r_{i\geq t}, s_{i>t} \sim E, a_{i\geq t} \sim \pi}[R_t | a_t, s_t] \tag{2.2}$$

$$Q^{\pi}(s_t, a_t) = \mathbb{E}_{r_{i\geq t}, s_{i>t} \sim E}[r(s_t, a_t) + \gamma \mathbb{E}_{a_{i>t} \sim \pi}[Q^{\pi}(s_{t+1}, a_{t+1})]] \tag{2.3}$$

Finally, an advantage function $A^{\pi}(s_t, a_t)$ is defined as the additional return or advantage that the agent will have for executing some action a_t at state s_t and it is given by $A^{\pi}(s_t, a_t) = Q^{\pi}(s_t, a_t) - V^{\pi}(s_t)$.

In high-dimensional state/action spaces, these functions are usually approximated by a suitable parametrization. Accordingly, we define θ^Q, θ^V, θ^A, θ^{π}, and θ^{μ} as the parameters for approximating Q, V, A, π, and μ functions, respectively. It was believed that using nonlinear function approximators for both Q and V functions would lead to unstable learning in practice. Recently, Mnih et al. [26] applies two novel modifications, namely *replay buffer* and *target network*, to stabilize the learning with deep nets. Later, several variants are introduced and extend deep architectures to learning tasks with continuous actions [39, 40, 46, 47].

To exhaustively analyze the effect of multi-sensor input on our proposed method, we pick two algorithms, namely Normalized Advantage Function (NAF) [39] and Deep Deterministic Policy Gradient (DDPG) [40], and augment them to accept multimodal inputs. It is worth noting that the two algorithms are very different, with DDPG being an off-policy actor-critic method and NAF an off-policy value-based one. By augmenting these two algorithms, we highlight that any DRL algorithm, modified appropriately, can benefit from using multiple inputs.

2.2.1 Continuous Action Space Algorithms

Normalized Advantage Function (NAF)

Q-learning [48] is an off-policy model-free algorithm, where agent learns an approximated Q function, and follows a greedy policy $\mu(s) = \arg\max_a Q(s, a)$ at each step. The objective function (2.1) can be reached by minimizing the square loss Bellman error

$$L = \frac{1}{N} \sum_{i}^{N} (y_i - Q(s_i, a_i | \theta^Q))^2 \tag{2.4}$$

where target y_i is defined as $r(s_i, a_i) + \gamma Q(s_{i+1}, \mu(s_{i+1}))$.

Deep Q-Network (DQN) parametrizes Q function with deep neural network [26], and has been shown to emulate human performance [27] in many Atari games using just image pixels as input. However, in these games, action choices are limited and discrete. Recently, Gu et al. [39] proposes a continuous variant of DQN by a clever network construction. The Q network, which they call Normalized Advantage Function (NAF), parameterizes the advantage function quadratically over the action space and is weighted by nonlinear features of states.

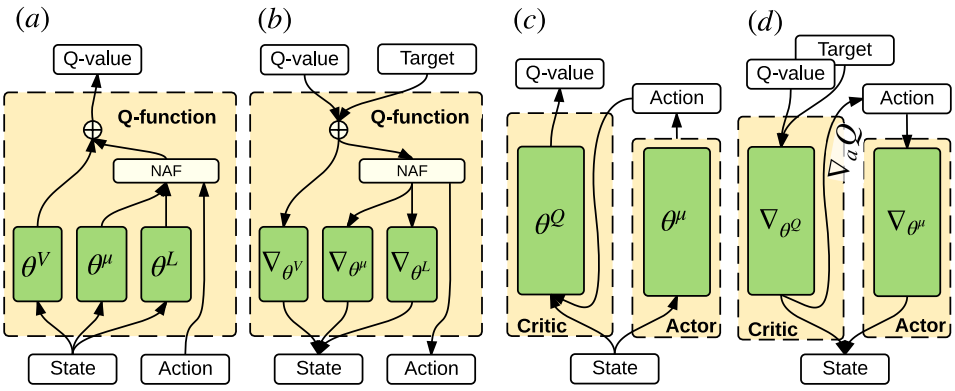

Figure 2.1: Schematic illustration of (a) forward and (b) back-propagation for NAF, and (c) forward and (d) back-propagation for DDPG. Green modules are functions approximated with deep nets.

$$Q(s,a|\theta^Q) = A(s,a|\theta^\mu,\theta^L) + V(s|\theta^V) \tag{2.5}$$

$$A(s,a|\theta^\mu,\theta^L) = -\frac{1}{2}(a-\mu(s|\theta^\mu))^T P(s|\theta^L) (a-\mu(s|\theta^\mu)) \tag{2.6}$$

$$P(s|\theta^L) = L(s|\theta^L)^T L(s|\theta^L) \tag{2.7}$$

During run-time, the greedy policy can be performed by simply taking the output of sub-network $a = \mu(s|\theta^\mu)$. The data flow at forward prediction and back-propagation steps are shown in Fig. 2.1 (a) and (b), respectively.

Deep Deterministic Policy Gradient (DDPG)

An alternative approach to continuous RL tasks is the actor-critic framework, which maintains an explicit policy function, often called *actor*, and an action-value function called *critic*. In [49], a novel *deterministic* policy gradient (DPG) approach is proposed. Silver et al. [49] shows that the objective function can be achieved using the policy gradient calculated from the gradient of the action-value function.

$$\nabla_{\theta^\mu} J = \mathbb{E}[\nabla_a Q(s,a|\theta^Q)\nabla_a \mu(s)] \tag{2.8}$$

Building on this result, Lillicrap et al. [40] proposes an extension of DPG with deep architecture to generalize their prior success with discrete action space [27] onto continuous space. Similar techniques as in [27] are utilized for stable learning. To explore the full state and action space, an exploration policy is constructed by adding Ornstein-Uhlenbeck noise process [50]. The data flow for prediction and back-propagation steps are shown in Fig. 2.1 (c) and (d), respectively.

2.3 Stochastic regularization

Stochastic regularization is an active area of research in deep learning made popular by the success of, *Dropout* [51]. Following this landmark paper, numerous extensions are proposed to further generalize this idea such as *Blockout* [52], *DropConnect* [53], *Zoneout* [54], etc. In the similar vein, two interesting techniques have been proposed for specialized regularization in the multimodal setting namely ModDrop [55] and ModOut [56]. Given a much wider set of sensors to choose from, ModOut attempts to identify which sensors are needed to fully observe the system behavior, which is out of the scope of this work. Here, we assume that all the sensors are critical and we only focus on improving the state information based on inputs from multiple observers. ModDrop is much closer in spirit to the proposed *Sensor Dropout (SD)*. However, unlike ModDrop, pre-training with individual sensor inputs using separate loss functions is not required. A network can be directly constructed in an end-to-end fashion and *Sensor Dropout* can be directly applied to the sensor fusion layer just like Dropout. Its appeal lies in its simplicity during implementation and is designed to be applicable even to the DRL setting. As far as we know, this is the first attempt at applying stochastic regularization in a DRL setting with the spirit of sensor fusion.

2.4 Deep Inverse Reinforcement Learning (DIRL)

As shown in Fig. 2.2, in the standard reinforcement learning, we are interested in learning the optimal policy that maximizes the total expected rewards collected from the environment. However, for some of the interesting problems in robotics fields, designing reward functions can be non-trivial and often requires lots of handy tunings. On the other hand, the consequences of the policy are usually relatively easy to observe. These problems fall in the category of *inverse* reinforcement learning (IRL) [57] (also imitation learning, learning from demonstration).

Given a set of expert demonstrations $D = \{\xi_i\}_{i=1}^{N}$, where each trajectory ξ_i consists of a sequence of state-action pair $\xi_i = \{(s_j, a_j)\}_{j=1}^{K}$, the goal of IRL is to infer the underlying reward function that leads to the policy π. We parametrize the reward function r with θ. Abbeel and Ng [58] proposes a strategy of matching feature expectations between the demonstration policy and the learner's behavior. Ratliff et al. [59] proposes a clever framework named *Maximum Margin Planning* (MMP), where learning to plan by mimicking the expert behavior is cast as a structured prediction problem. Under the structured margin criteria, the objective can be formulated in the following form:

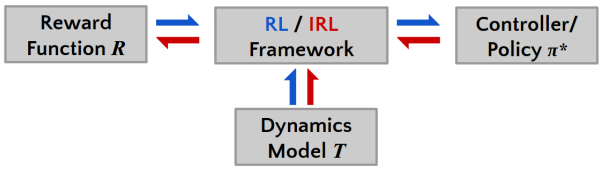

Figure 2.2: The block diagram of reinforcement learning and inverse reinforcement learning.

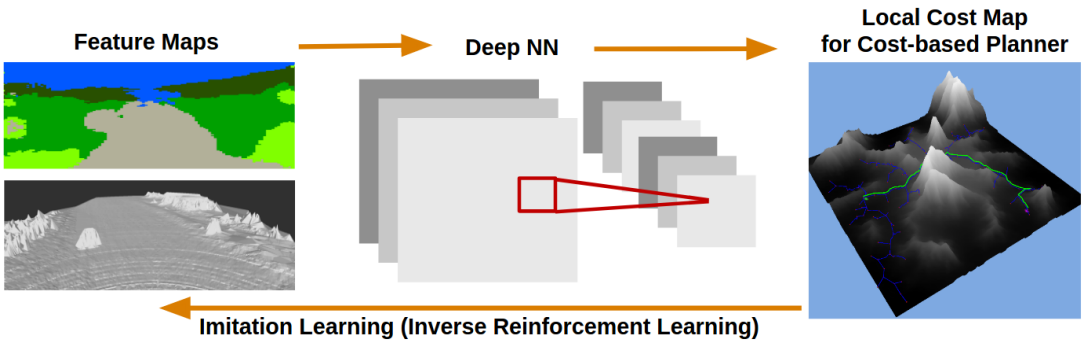

Figure 2.3: Schematic illustration of deep inverse reinforcement learning.

$$L(\theta) = \frac{1}{N}\sum_{i=1}^{N} \beta_i (\max_{\mu \in \mathbb{G}_i} (\theta^T F_i + l_i^T)\mu - \theta^T F_i \mu_i)^q + \frac{\lambda}{2}\|\theta\|^2 \tag{2.9}$$

Here, μ_i, F_i, and l_i represent the state visited frequencies (SVF), feature matrix, and margin loss vector of the i^{th} trajectory, respectively. Note that Eq. 2.9 assumes the linearity constraint on the reward function. The parameter θ is optimized in a way that minimizes the q-norm mean losses between the optimal trajectory under the loss-augmented reward structure and the demonstration trajectories. The loss vector alleviates the ill-posed problem in the IRL [58], where a trivial solution like all-zeroed weights guarantees all policies to be optimal. The intuition behind MMP implies the resulting solution should look significantly better than the alternative policies.

However, both approaches fail to capture the ambiguity of the observed policies. It is worth mentioning that for complex problems such as off-road navigation and racing planning, the assumption on the optimality of the demonstrations is indeed strong. In fact, the optimal policy is usually unknown, and the behavior may differ from each expert player. Specifically, when the demonstrations are imperfect, or the planning algorithms capture only part of the relevant feature space, the resulting reward function from the previous approaches cannot perfectly describe the observed trajectories. In this light, Ziebart et al. [60] reformulates the problem under the principle of maximum entropy. The resulting algorithm, known as maximum entropy IRL (ME-IRL), models the demonstrations with a stochastic policy by assuming the probability of executing of each trajectory being exponentially proportional to its total accumulated rewards.

$$P(\xi_i|r_\theta) = \frac{1}{Z}\exp\left(r_\theta(\xi_i)\right) \tag{2.10}$$

$$\text{,where} \quad Z = \sum_{\xi \in \Xi} \exp\left(r_\theta(\xi)\right) \text{ is the normalization constant.} \tag{2.11}$$

The gradient of the objective function under linear reward function is simply the difference between the expected empirical feature counts and the learner's expected feature counts.

Recently, Wulfmeier et al. [42] shows that the gradient calculated in ME-IRL can be naturally extended to the back-propagation in the standard deep supervised learning. By re-framing the problem with standard Bayesian inference as a MAP estimation problem, the objective function is simply:

$$L(\theta) = \log P(D, \theta | r) = \log P(D|r) + \log P(\theta) \tag{2.12}$$

The negative log-likelihood contains two terms: the data term L_D and a standard weight decay term L_θ as the regularization. The gradient of the first term is simply:

$$\frac{\partial L_D}{\partial \theta} = \frac{\partial L_D}{\partial r} \frac{\partial r}{\partial \theta} \tag{2.13}$$

$$= (\mu_D - \mathbb{E}[\mu]) \cdot \frac{\partial r}{\partial \theta} \tag{2.14}$$

Note the gradient degenerates to ME-IRL if the reward function is linear on feature space. If the reward function r is approximated by a deep network, the latter term $\partial r / \partial \theta$ can be calculated efficiently using back-propagation, and the objective function can be optimized with gradient-based approaches. This framework, called deep maximum entropy deep inverse reinforcement learning (ME-DIRL or simply DIRL) has been successfully applied to urban autonomous navigation in [43]. The schematic illustration of the DIRL is summarized in Fig. 5.1.

Chapter 3

Model Predictive Planning

In this chapter, we propose a model-based local planner for high-speed maneuvering in the off-road navigation application. To overcome the highly unpredictable vehicle dynamics in the unstructured terrain, we derive our vehicle model in a data-driven fashion. The high-dimensional vehicle model is used as a standpoint of our model-predictive local planner.

The local planner is constructed with Rapidly-exploring Random Tree (RRT) [21] as its template. Though sample-based algorithms are generally more suitable for high-dimensional state space planning, it is not straightforward to extend to kinodynamic planning. To operate the planning process in control space, our planner slightly departs from the standard RRT to perform a certain level of trajectory optimization given the limited computational cycle. A cost function is designed using traveling time to encourage the vehicle for a more aggressive maneuvering.

We use height map algorithm to efficiently process the incoming cloud point data and detect collisions in the future. The potential obstacles are accumulated on a simplified occupancy grid to produce a collision check grid map. Finally, the proposed planner is tested on a full-size all-terrain vehicle (ATV) in the off-road environment. We show that our planner can perform smooth yet aggressive movements to avoid static obstacles with high speed up to $30kph$.

The chapter is organized as follows: Section 3.1 summarizes the derivations of two vehicle models. In Section 3.2, we introduce our sample-based planner and detail technical implementations. Finally, Section 3.1 shows the experimental results and the videos of high-speed navigation.

3.1 Vehicle Response Model

The forward predictive model $\dot{x} = f(x, u)$ is defined as a function that maps a pair of control action $u \in \mathcal{A}$ and state $x \in \mathcal{S}$ to the next state. As shown in Fig. 3.1a, in our application, the control space consists of the $2DOF$ executed velocity command, *i.e.* forward and rotational velocity, and the state space consists of the actual velocity responses in $2D$ plane, *i.e.* $[v_x, v_y, w]$, in the local frame. It is worth mentioning that the sliding velocity v_y is not negligible on the rough terrain, and in fact plays a crucial role in the off-road environment.

Previous works [61, 62, 63] formulate the predictive models for unmanned ground vehicles (UGV) in a modular fashion, where specialized algorithms are developed for each subsystem

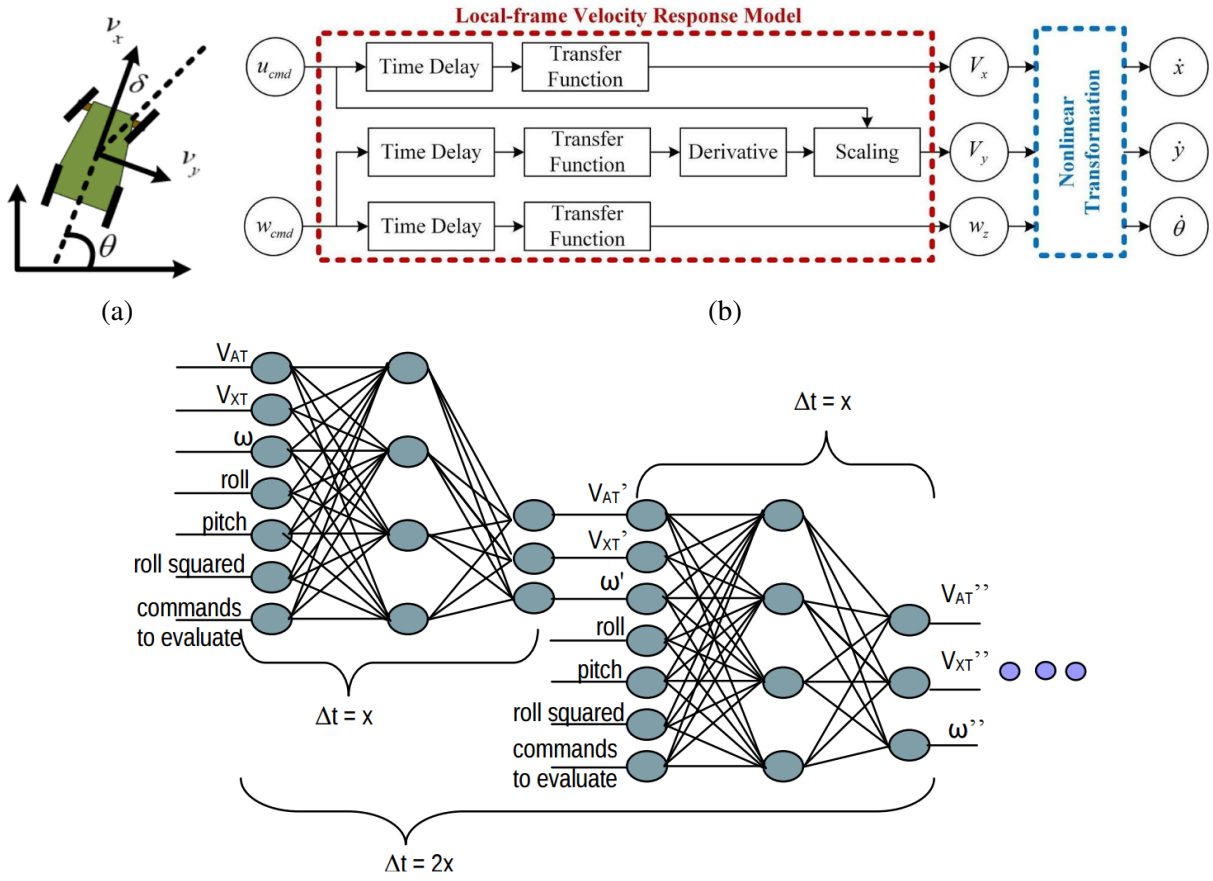

Figure 3.1: (a) Notation of vehicle velocity in local frame. (b) Data flow of conventional dynamic response model. The model takes two velocity control commands as input and estimates the velocity response in vehicle frame. (c) Schematic illustration of neural network based response model from [6].

and later integrated with some fine tunings. Though this approach offers rich semantic representation to allow researchers to better examine the performance of each module, modeling subsystems such as actuator dynamic, vehicle suspension model, and wheel-terrain interaction can be very complex and computationally expensive. Here, we limit our scope to a more intuitive yet effective method; instead of modularizing the process where the accumulating errors due to the imperfect approximations may propagate and scale up to harm the overall performance, we approximate the predictive model in a more end-to-end fashion.

We derive the model with two different approaches. The first approach derives the transfer function based on the standard system identification process. The forward and angular velocity responses, *i.e.* $v_x(t)$ and $w_z(t)$, take the forward and angular velocity commands as inputs, respectively. The lateral velocity response, on the other hand, uses both commands as input. Our observation is that the UGV experiences lateral sliding whenever the rotational speed changes, with the magnitude of the angular acceleration being proportional to the forward velocity. The

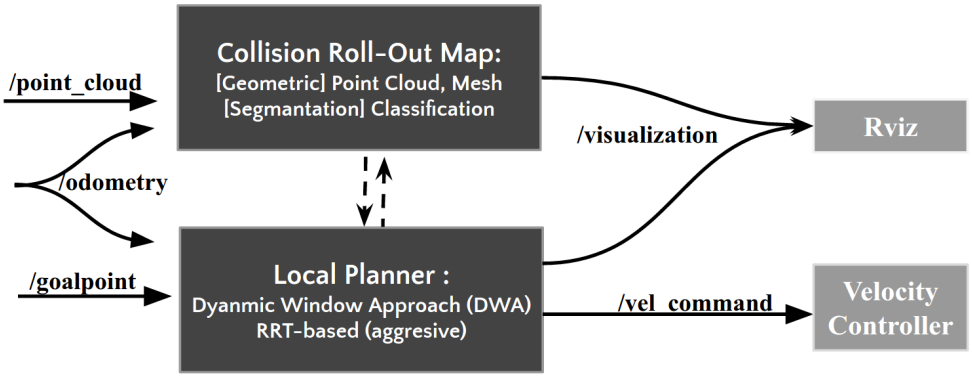

Figure 3.2: Block Diagram of our planner API.

corresponding block diagram is summarized in Fig. 3.1b. The relative position with respect to the origin in local frame can be calculated by integrating through velocity space.

For the second approach, we implement the neural network model based on previous work [6]. As shown in Fig. 3.1c, the neural network takes additional information, such as roll, pitch, and yaw angle, as its input. Note that the squared roll angle is also provided because, from a dynamics standpoint, the vehicle should respond in a near symmetrical manner if it is rolled to the right or rolled to the left. We refer two models as *Conventional Dynamic Model* and *NNet Model* for convenience in the later section.

3.2 Planner Design

The block diagram of our planner is shown in Fig. 3.2. It can be separated into two modules with respect to functionality. The collision check module constructs a global simplified occupancy grid given the point cloud data and the odometry. The local planner module takes the odometry and the goal state as inputs, performs minimal calculations, and finally sends the velocity commands directly to the onboard velocity controller. The two modules interact with each other in the way that the local planner acquires collision detections from the roll-out map. The detail of two modules is described as follows:

3.2.1 Collision Check Module

Occupancy grid is a commonly-used data structure for obstacles detection. It stores one or multiple probabilities in each grid cell and increases or decreases them based on sensor model. Since our testing scenario is relatively flat without noise, a simplified version of occupancy grid is used in the matter of fast implementation, in which we replace the probabilities with a counter. Three different methods for obstacles segmentation are investigated and described below:

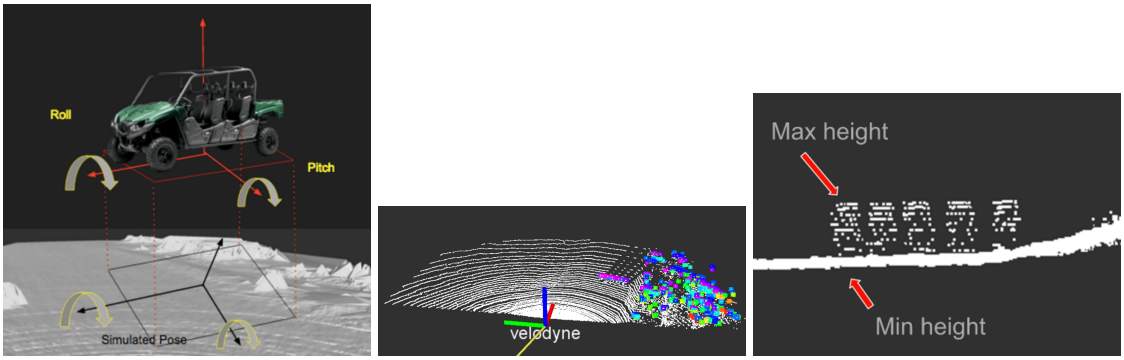

(a) Mesh with ODE simulation (b) RANSAC segmentation. (c) Height map algorithm

Figure 3.3: Three different methods of collision check. Note that for (b), the original and the processed point cloud is represented by white and colored dot, respectively.

i. Mesh Representation with Simulation in Open Dynamic Engine (ODE) [64]

The original method implemented on the vehicle uses ODE and mesh data to simulate the vehicle pose on the ground. The collision is reported if 1) an intersection is detected between the vehicle and the mesh map or 2) the simulated roll or pitch angle is beyond the user-defined thresholds.

ii. Plane Removal with RANSAC Segmentation [65]

The second approach for collision check module is using RANSAC segmentation from Point Cloud Library (PCL) to fit the plane model. In our case, the plane model is the ground of our testing environment. We extract the outliers from RANSAC for obstacle detection. As shown in Fig. 3.3b, the white point cloud is the original data, while the colored point cloud is the outliers from RANSAC.

iii. Height Map Algorithm

The third method we used is height map algorithm, which is a simple yet efficient algorithm regarding computation. It calculates the height differences within one grid. If the height difference is greater than a user-defined threshold, the obstacle is categorized as an obstacle. As shown in Fig. 3.3c, since the artificial obstacle is approximately 1.5 meters, we set the threshold to be 1 meter.

Since collision check is the most computationally expensive part of our system and we cannot afford to collide our platform with the obstacles, efficiency and reliability are the most important requirements. Though the mesh representation is a good approach for future application, it is not feasible in our scenario regarding computation consumption. The RANSAC segmentation, on the other hand, is sensitive to off-road conditions; the plane model cannot be perfectly fit on rough terrain. In addition, the dusty environment in off-road driving creates noises and interferences to the Lidar. Considering our requirements and the discussion mentioned above, we choose height map algorithm as our final approach. It is the fastest and the most reliable. Furthermore, to

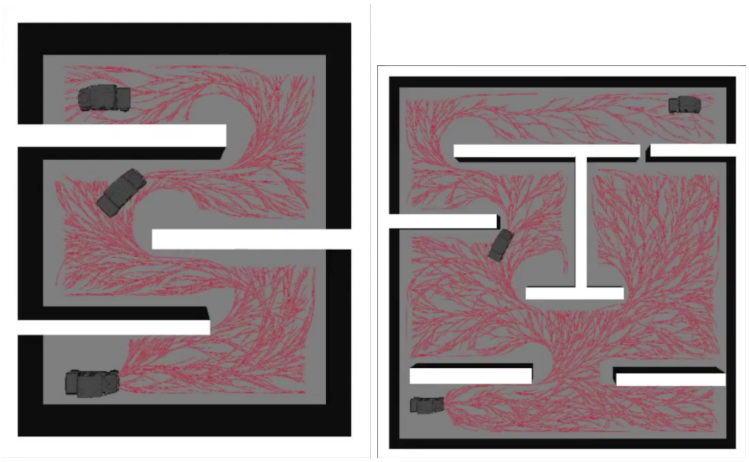

(a) (b)

Figure 3.4: Simulation of RRT planner with vehicle model derived in Sec. 3.1

Table 3.1: Simulation Benchmark

	PDST [66]	EST [67]	RRT [21]	KPIECE [68]
TIME	15.04	15.05	**15.03**	15.07
SOLUTION CLEARANCE	1.63	1.54	**1.38**	1.70
SOLUTION DIFFERENCE	1.05	1.11	**0.98**	1.30

optimize the computing efficiency, we use bitwise operation instead of multiplication and dilate the obstacle size to increase the robustness of our system.

3.2.2 Sample-based Planner Module

Instead of using traditional search-based planners such as **A*** or **D***, we use a sample-based planner as our development platform. This critical choice comes from an insight that sample-based planner is more efficient for solving a high-dimensional planning problem, which gives us a powerful tool when we want to utilize a more complex dynamic vehicle model for state propagation.

Simulation

Our planner is built upon Open Motion Planning Library (OMPL) [69], an open-source motion planning library that includes a broad range of sample-based planners and a built-in simulation platform called *OMPL.app*. The template of the sampled-based planner is determined from simulations where we generate mazes scenarios and implement the vehicle response model on several available off-the-shelf planners. Table 3.1 summarizes the simulated benchmark result, while Fig. 3.4 shows the simulation environments. The demo video available at `http://ppt.cc/sBLAh`. We observe that the RRT algorithm gives a faster solving time and a smaller path

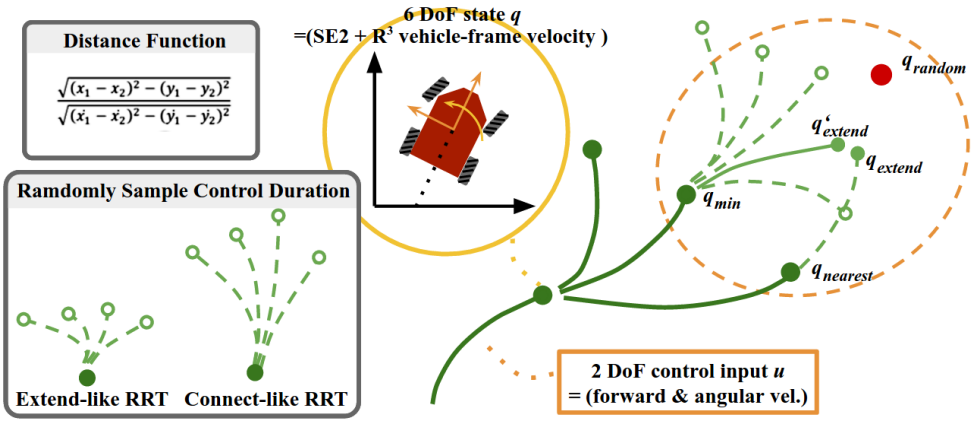

Figure 3.5: The visualization of RRT-based planner.

clearance under our vehicle model constraints. With other advantages such as flexibility and extendibility, we use RRT as our planner template and extend it for our purpose.

Implementation Details

Fig 3.5 visualizes the RRT tree. Each node represents a 6 DoF state, $q = [x, y, \theta, v_{forward}, v_{sliding}, w]^T$. The first three terms represent the state in standard SE2 space, and the last three terms stand as the velocity in vehicle frame on a 2D plane. For control space, we follow the convention used in Section 3.1, which includes $2DOF$ forward and angular velocity.

After a random state q_{random} is sampled, RRT extends its leaf by determining a sequence of control input and its operation duration toward an extended state q_{extend}. To perform a smooth control throughout the trajectory for off-road navigation, we first uniformly sample the forward velocity command within an adjustable region. This command region is determined at run-time based on the previously issued commands, current vehicle status, and previously executed path so that the vehicle will hold the velocity consistency without jerky output. Then, the shooting method is used to determine the angular velocity command.

As shown in the dotted circle in Fig. 3.5, the basic RRT-like algorithm preserves a fixed extended step size throughout planning time. While using a larger step size may decrease solving time yet result in a jerky trajectory, the trajectory propagated with a smaller step size is usually smoother but computationally expensive. The former one is usually referred to *Connected RRT*, and the latter one is called *Extended RRT*. In our implementation, instead of fixing the control duration as a hyper-parameter, we randomly sample the control duration. Our motivations come from the results of our maze simulations, where we observe that tuning the control duration greatly affects the planner performance in different maze configuration. We believe loosening the step size constraint with such random sample mechanism will generalize our planner for various situations encountered in off-road environments.

Optimal kinodynamic motion planning for a sample-based planner can be very computationally expensive. As described in Section 2.1, moving from RRT toward RRT* includes two more optimization steps in each iteration: (1) reconnecting to an extended state, and (2) tree edges

Table 3.2: Planner Hyper-parameter

GOAL BIAS		0.7
PLANNER RATE		2 HZ
SOLVING RATE		20 HZ
CONTROL DURATION		1.5–6 SEC
CONTROL INPUT	FORWARD	10–30 KPH
	ANGULAR	-0.5–0.5 RAD/S

trimming. Here, we implement a time-optimal RRT* algorithm motivated from hwan Jeon et al. [22]. However, only the first of two optimization steps is applied because the trimming process includes updating the whole children tree, which will trade off with planning time. The extend function in the first procedure is implemented slightly different from the basic version in that instead of connecting q_{extend} directly to q_{min}, we apply shooting method and replace q_{extend} with $q^{''}_{extend}$. The intuition is that it is nearly impossible to propagate to the *same* node in 6 DoF state space with arbitrary control commands. The replacement of q_{extend} is accepted only if the new state $q^{''}_{extend}$ is close enough to q_{extend}. Finally, we also follow the same setting by using the traveling time instead of standard Euclidean distance as the cost function. The planner thus optimizes the trajectory by minimizing the traveling time and is encouraged to maneuver agilely under the dynamics constraints.

The re-planning process is designed as follows: at the beginning of each planner loop, the vehicle status, collision check map, and goal state are updated to formulate an RRT control-space planning problem. The problem is solved multiple times, and the best solution in each iteration is stored. When the computational time exceeds, the solution with minimal cost is outputted for execution. Note that the growth tree is abandoned when the next solving iteration starts. In practice, such design helps prevent the planner from publishing poor solution if bad tree structure is built at the beginning of growth stage. We admit that if an optimal solution can be obtained from one single shot, the re-planning setting would have changed significantly [70]. It is also worth mentioning that there is a time delay between the time when the vehicle status is updated and the time when the velocity command generated by RRT-based planner is executed. To effectively capture the latency, the starting vehicle state, *i.e.* the root of RRT, is simulated by propagating the current vehicle with the delayed time using the vehicle model derived in the previous section. The parameters used in our local planner are listed in Table 3.2.

3.3 Experiments and Analysis

We use Yamaha Viking VI side-by-side ATV as our main testing platform. As shown in Fig. 3.6, the vehicle is equipped with the custom drive-by-wire system, velocity controller, and navigation sensors such as GPS/INS, LiDAR, and RGB-D camera.

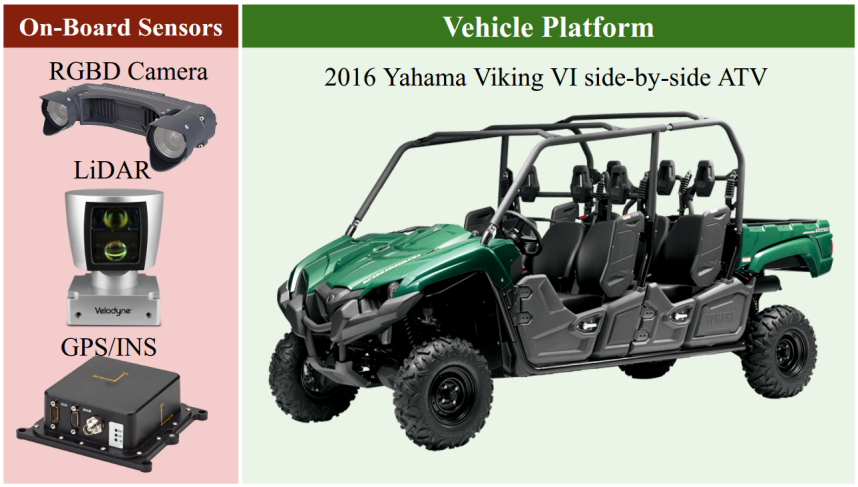

Figure 3.6: The testing vehicle platform and the onboard sensor.

3.3.1 Vehicle Model Verification

Fig. 3.7 shows the simulated velocity, while Fig. 3.8 shows the integrated relative position. The differences between the blue and red line reflect the complexity of vehicle model on the unstructured terrain. Integrating directly from control command through time, as shown with the blue line, will give a poor result on state propagation. Both two proposed models are capable of estimating the lateral velocity, which plays a non-negligible role in off-road cases. However, the conventional dynamic model is not capable of capturing the nuance variation of the forward velocity. The neural net model, on the other hand, gives a better estimation.

3.3.2 Planner Demo

We test our planner on an off-road test field located near Gascola, Penn Hills, PA. Our testing scenario is designed as followed: the vehicle should autonomously navigate through a straight turnpike where multiple static obstacles are placed alternatively on both side of the track. Each static obstacle is 3-meter-length and 1.5-meter height. The turnpike is a rectangle-shaped field with 10-meter width and 150-meter length. The fastest way to go through the obstacles without any collisions is to perform S-shape maneuvering. Since the standard operating speed ranges from 10 to $40kph$, we set the baseline testing speed as $20kph$ with the top speed of $30kph$.

As shown in our demo video [1], the vehicle can successfully avoid all the obstacles at $25kph$. However, driving at higher speed ($\sim 30kph$) sometimes makes collision map vulnerable to noises such as dust and sand blown up when the vehicle drives through, which highly affect the path quality outputted by the planner. The example of planning path generation is visualized in Fig. 3.9.

[1] On-field testing with path visualization: `https://youtu.be/LibnO8_Sjm0`

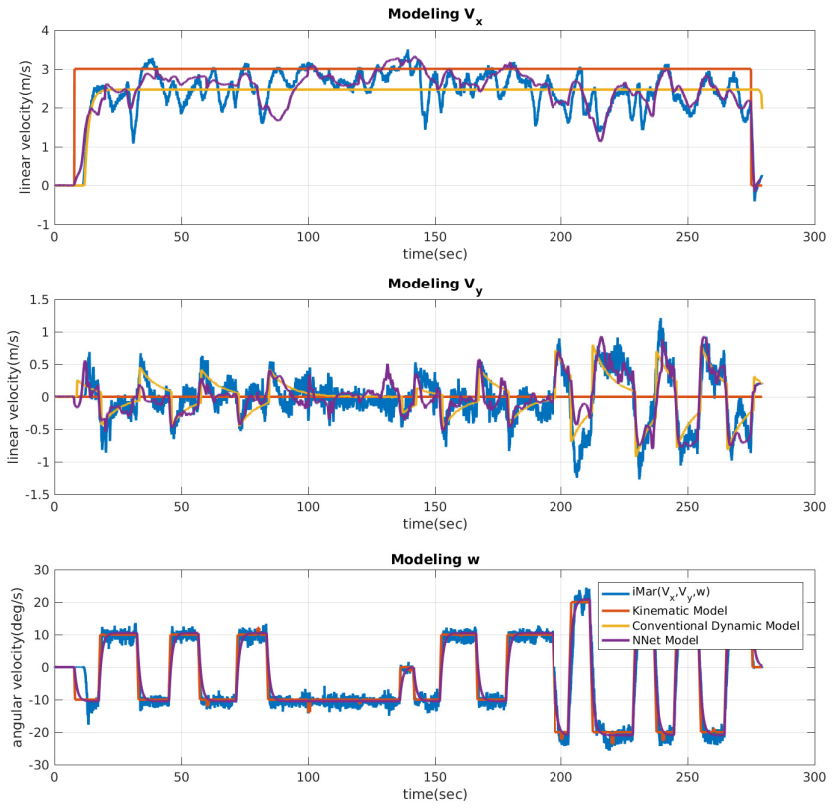

Figure 3.7: Simulated velocity response w.r.t. time steps. Note that the blue line is measured under an accurate GPS/INS sensor with RTK signal. We refer this measurement as our ground true data.

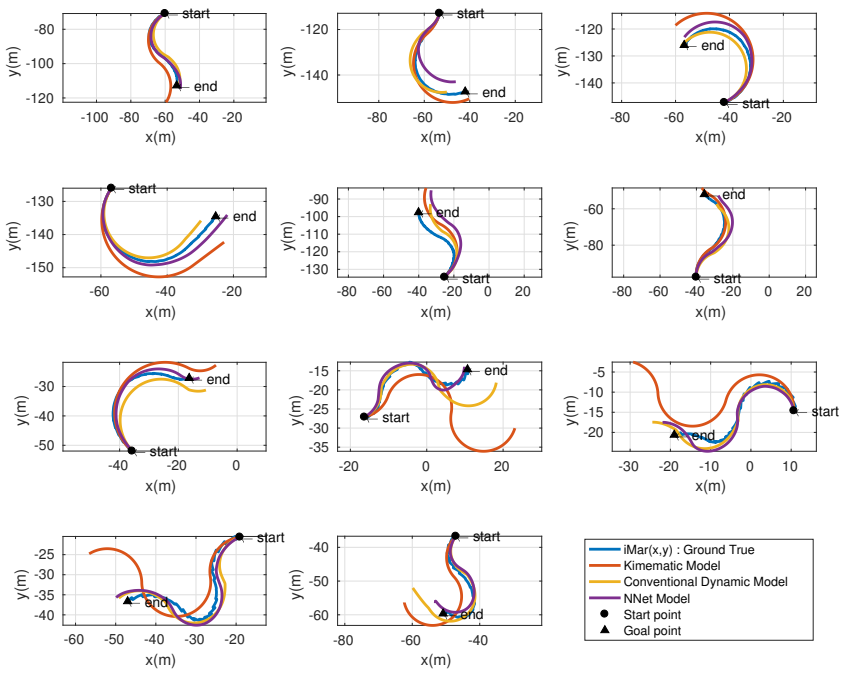

Figure 3.8: Comparison between data-driven dynamic model and original kinematic model. Note the time interval in each graph is 20 seconds.

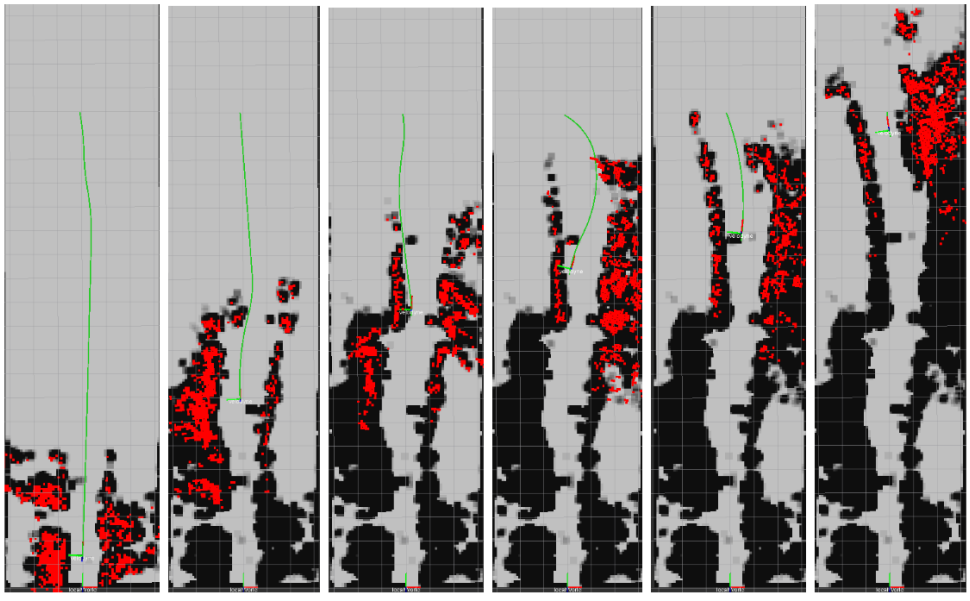

Figure 3.9: Screenshots of planner visualization output. The green path is the trajectory where each point is encoded with a 6 DoF state, 2 DoF control input, and a control duration. The red points are the filtered point cloud segmented as obstacles.

Chapter 4

Learning End-to-end Multimodal Sensor Policy

In this chapter, we present an alternative end-to-end controller that maps the multi-sensor input directly to the action space based on deep reinforcement learning (DRL), a recently popular research field. We propose two novel methods that effectively train the multimodal sensor policy without over-fitting to partial sensor subset, namely *Sensor Dropout* and *Auxiliary Loss*. Two popular continuous action DRL algorithms namely Normalized Advantage Function (NAF) [39] and Deep Deterministic Policy Gradient (DDPG) [40], are picked and augmented to accept multimodal input. The resulting autonomous navigation policy is tested exhaustively to verify its performance in a physics-based gaming environment called TORCS [38].

Through extensive empirical testing, we show the following exciting results,

1. Multimodal-DRL with Sensor Dropout(SD) reduces performance drop in a noisy environment from $\approx 40\%$ to just 10% when compared to a baseline single sensor system.
2. Policies learned using SD best leverage the multimodal setting by greatly reducing over-dependence on any one sensing modality. Additionally, for each sensor, we observe that SD enforces sparsity and promotes each sensor to base the policy primarily on intuitive and salient features.
3. A multimodal sensor policy with SD guarantees functionality even in a face a sensor failure, which is a huge plus and the best use-case for the need for redundancy in a safety-critical application like autonomous navigation.

The chapter is organized as follows: Section 4.1 introduces two methods on effectively training a multimodal sensor policy. We first introduce a new stochastic regularization called Sensor Dropout and details its advantages over the standard Dropout for this problem. The resulting policy can be further fine-tuned by adding additional auxiliary losses to reduce the action variance. The performance of Sensor Dropout is then validated in Section 4.2. In Section 4.3, we summarize our results and discuss key insights obtained through this exercise.

4.1 Proposed Methods

Multimodal DRL aims to leverage the availability of multiple, potentially imperfect, sensor inputs to improve learned policy. Most autonomous driving vehicles have been equipped with an array of sensors like GPS, Lidar, Camera, and Odometer, etc [71]. While one would offer a long range noisy estimate, the other would offer a shorter range accurate one. When combined though, the resulting observer will have a good and reliable estimate of the environment. This problem is critical as a further step toward the real-world robotics application given the current state-of-the-art DRL agents on many realistic simulators.

4.1.1 Multimodal Network Architecture

We denote a set of observations composed from M sensors as, $S = [S^{(1)}\ S^{(2)}\ ..\ S^{(M)}]^T$, where $S^{(i)}$ stands for observation from i^{th} sensor. In the multimodal network, each sensory signal is pre-processed along independent paths. Each path has a feature extraction module with an appropriate network architecture, using randomly initialized or pre-trained weights. In this work, we use three different inputs namely image, laser scan and physical parameters (like wheel speed, position, odometry, etc. The details of each of the feature extraction module are listed in the Appendix. The modularized feature extraction stages for multiple inputs naturally allows for independent extraction of salient information that is transferable (with some tuning if needed) to other applications like collision avoidance, pedestrian detection, and tracking, etc. The schematic illustration of modularized multimodal architecture is shown in Fig. 4.1. The outputs of feature extraction modules are eventually flattened and concatenated to form the multimodal state.

4.1.2 Sensor-based Dropout (SD)

The Sensor Dropout (SD) is a variant of the vanilla Dropout [51] that maintains dropping configurations on each sensor module instead of an individual neuron. Though both methods share a similar motivation on stochastic regularization, SD is better-motivated for training the multimodal sensor policy. By randomly dropping the sensor block during training, the policy network is encouraged to exploit the modularized structure among each sensor stream. In the application to the complex robotics system, SD has advantages on handling imperfect conditions such as latency, noises, and even partial sensor failure.

As shown in Fig.4.1, consider the multimodal state $\tilde{S}$, obtained from feature extraction and given by $\tilde{S} = [\tilde{S}^{(1)}\ \tilde{S}^{(2)}\ ..\ \tilde{S}^{(M)}]^T$, where $\tilde{S}^{(i)} = [\tilde{X}_1^{(i)}\ \tilde{X}_2^{(i)}\ ..\ \tilde{X}_{K_i}^{(i)}]^T$. The dropping configuration is defined as a M-dimensional vector $\mathbf{c} = [\delta_c^{(1)}\ \delta_c^{(2)}\ ..\ \delta_c^{(M)}]^T$, where each element $\delta_c^{(i)} \in \{0, 1\}$ represents the on/off indicator for the i^{th} sensor modality. We now detail the two main differences between original Dropout and SD along with their interpretations.

Firstly, note that the dimension of the dropping vector $\mathbf{c}$ is much lower than the one in the standard Dropout ($\sum_{i=1}^{M} K_i$). As a consequence, the probability of the event where all sensors are dropped out (*i.e.* $\mathbf{c_0} = [0^{(1)}\ 0^{(2)}\ ..\ 0^{(M)}]^T$) is not negligible in SD. To explicitly remove $\mathbf{c_0}$, we slightly depart from [51] in modeling the SD layer. Instead of modeling SD as a random process where any sensor block $\tilde{S}^{(i)}$ is switched on/off with a *fixed* probability p, we define the

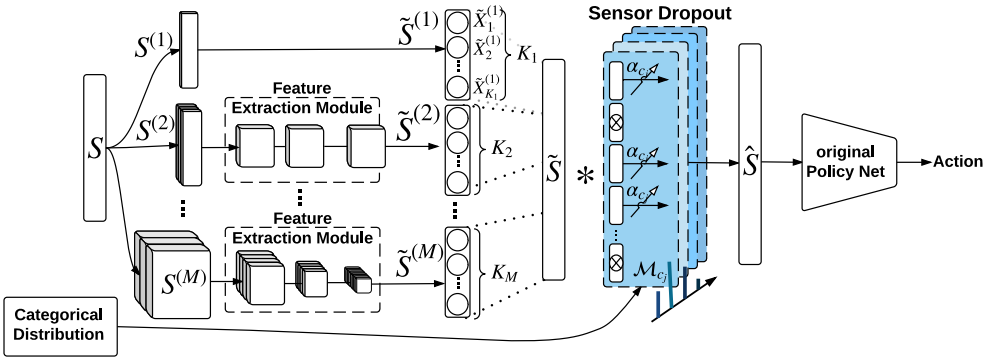

Figure 4.1: Illustration of multimodal sensor policy network augmented with Sensor Dropout. The operation $*$ stands for element-wised multiplication. The dropping configuration of Sensor Dropout is sampled from a categorical distribution, which the network takes as an additional input. The feature extraction module can be either pure identity function (modality 1), or convolution-based layer (modality $2 \rightarrow M$). The operation $\odot *$ stands for element-wised multiplication.

random variable as the dropping configuration $\mathbf{c}$ itself. Since there are $N = 2^M - 1$ possible states for $\mathbf{c}$, we accordingly sample from an N-state categorical distribution $\mathbb{P}$. The categorical distribution not only offers convenience in analysis and interpretation over standard Bernoulli on sensor blocks, but is better-motivated in that it can be adaptive to the current sensor reliability during run-time. We denote the probability of a dropping configuration $\mathbf{c_j}$ occurring with p_j, where the subscript j ranges from 1 to N. The corresponding pseudo-Bernoulli [1] distribution for switching on a sensor block $\tilde{S}^{(i)}$ can be calculated as $p^{(i)} = \sum_{j=1}^{N} \delta_{c_j}^{(i)} p_j$.

Another difference from the standard Dropout is the rescaling process. Unlike the standard Dropout which preserves a *fix* scaling ratio after dropping neurons, the rescaling ratio in SD is formulated as a function of the dropping configuration and sensor dimensions instead. The intuition is to keep the weighted summations equivalent among different dropping configurations in order to activate the later hidden layers. The scaling ratio is calculated as $\alpha_{c_j} = \frac{\sum_{i=1}^{M} K_i}{\sum_{i=1}^{M} \delta_{c_j}^{(i)} K_i}$. In summary, the output of SD for the k^{th} feature in i^{th} sensor block (*i.e.* $\tilde{S}^{(i)}$) given a dropping configuration $\mathbf{c_j}$ can be shown as,

$$\hat{S}_{c_j,k}^{(i)} = \mathcal{M}_{c_j}^{(i)} \tilde{X}_k^{(i)}, \qquad \text{where } \mathcal{M}_{c_j}^{(i)} = \alpha_{c_j} \delta_{c_j}^{(i)}. \tag{4.1}$$

$\mathcal{M}_{c_j}^{(k)}$ is an augmented mask encapsulating both dropout and re-scaling.

[1] We wish to point out that $p^{(i)}$ is pseudo-Bernoulli as we restrict our attention to cases where at least one sensor block is switched on at any given instant in the layer. This implies that, while the switching on of any sensor block $\tilde{S}^{(i)}$ is independent of the other, switching off is not. So the distribution is no longer fully independent.

4.1.3 Augmenting Auxiliary Loss

An alternative interpretation of the SD-augmented policy is that sub-policy induced by each sensor combination are jointly optimized during training. Denote the ultimate policy and sub-policy induced by each sensor combination as $\mu_{\mathbf{c}\sim\mathbb{P}}$ and μ_{c_j}, respectively. The final output maintains a geometric mean over N different actions.

Although the expectation of the total policy gradients for each sub-policy is the same, SD provides no guarantees on the consistency of these actions. To encourage the policy network to extract salient features from each sensor that can be embedded with similar representation in the policy network, we further augment an auxiliary loss that penalizes the inconsistency among μ_{c_j}. This additional penalty term provides an alternative gradient that reduces the variation of the ultimate policy, *i.e.* $Var\left[\mu_{\mathbf{c}\sim\mathbb{P}}\right]$.

The mechanism is motivated from the recent successes [34, 72, 73, 74] that exploit how adding the auxiliary tasks help greatly improve both agent's performance and convergence rate. However, unlike most previous works that pick up the auxiliary tasks carefully from the ground truth environment, we formulate the *target action* from the policy network itself. Under the standard actor-critic architecture, the target action is defined as the sub-policy $\tilde{\mu}_{c^*}$ among target actor network $\tilde{\mu}_{\mathbf{c}\sim\mathbb{P}}$ that maximize the target critic values $\tilde{Q}$.

$$L_{aux} = \lambda \sum_{i=1}^{N} (\mu_{c_j}(s_i) - \tilde{\mu}_{c^*}(s_i))^2 \tag{4.2}$$

$$\text{where } c^* = \underset{c_j\sim\mathbb{P}}{\operatorname{argmax}} \sum_{i=1}^{N} \tilde{Q}(s_i, \tilde{\mu}_{c_j}(s_i)) \tag{4.3}$$

Here, λ is an additional hyperparameter that indicates the importance ratio between the two losses, and N is the batch size for off-policy learning.

4.2 Evaluation and Analysis

In this section, we outline our experimental setup using TORCS simulator and then exhaustively compare the performance of the trained policies on both DDPG and NAF algorithms with and without Sensor Dropout. The exhaustive analysis includes policy robustness, sensitivity, and dependency on each sensor modality. Finally, we use a perturbation-based technique to visualize the learned policies and finally discuss some of the interesting findings of this exercise. [2]

4.2.1 Platform Setup

TORCS Simulator The proposed approach is verified on TORCS [38], a popular open-source car racing simulator that is capable of simulating physically realistic vehicle dynamics as well as multiple sensing modalities [75] to build sophisticated AI agents. To make the learning problem representative of the real-world setting, we picked the following sensors from the TORCS package: the 2D laser range finder, front-view camera with RGB channel, and vehicle state - position

[2] A demo video can be seen here: `https://youtu.be/HC3TcJjXf3Q`

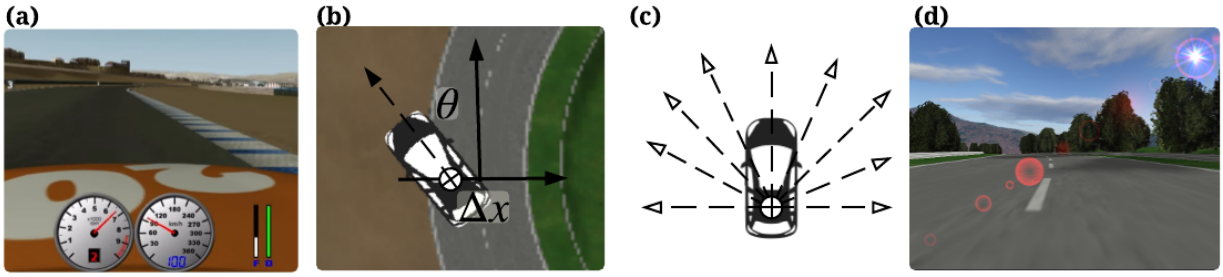

Figure 4.2: Sensors used in the TORCS racing car simulator: *Sensor 1:* Physical information such as velocity (a), position, and orientation (b), *Sensor 2:* Laser range finder (c), and *Sensor 3:* Front-view camera (d).

and speed. The action space is a continuous vector in $\mathbb{R}^2$, whose elements represent steering angle, and acceleration.

As shown in Fig. 4.2, the physical state is a 10 DOF hybrid state, including 3D velocity (3 DOF), position and orientation with respect to track centerline (2 DOF), and finally rotational speed of 4 wheels (4 DOF) and engine (1 DOF). Each laser scan is composed of 19 readings spanning a 180° field-of-view in the front of the car. Finally, the camera provides RGB channels with resolution 64×64. We use the following sensing modalities for our state description: (1) We define *Sensor 1* as a hybrid state containing physical-based information such as odometry and simulated GPS signal. (2) *Sensor 2* consists of 4 consecutive laser scans (*i.e.*, at time t, we input scans from times $t,\ t-1,\ t-2$ & $t-3$). Finally, as *Sensor 3*, we supply 4 consecutive color images capturing the car's front-view. These three representations are used separately to develop our baseline uni-modal sensor policies. The multimodal state, on the other hand, has access to all sensors at any given point. When Sensor Dropout (SD) is applied, an agent will randomly lose access to a strict subset of sensors. The categorical distribution is initialized with a uniform distribution among total 7 possible combinations of sensor subset, and the best-learned policy is reported here.

An exploration strategy is injected adding an Ornstein-Uhlenbeck process noise [50] to the output of the policy network. The choice of reward function is slightly different from Lillicrap et al. [40] and Mnih et al. [46] as an additional penalty term to penalize sideways drifting along the track is added. In practice, this modification leads to more stable policies during training [76].

Network Architecture For laser feature extraction module, we use two $1D$ convolution layers with 4 filters of size 4×1, while image feature extraction is composed of three $2D$ convolution layers: one layer of 16 filters of size 4×4 and striding length 4, followed by two layers each with 32 filters of size 2×2 and striding length 2. Batch normalization is followed after every convolution layer. All these extraction modules are fused and are later followed up with two fully-connected layers of 200 hidden units each. All hidden layers have *relu* activations. The final layer of the critic network use *leaner* activation, while the output of the actor network is bounded using *tanh* activation. We use sigmoid activation for the output of L network in NAF. In practice, it leads to a more stable training for high dimensional state space. We trained with

Table 4.1: Model Specification

Model ID	State Dimensionality	Description
Physical	10	
Lasers	4×19	4 consecutive laser scans
Images	$12 \times 64 \times 64$	4 consecutive RGB image
Multi	$10{+}1{\times}19{+}3{\times}64{\times}64$	all sensor streams at current time step

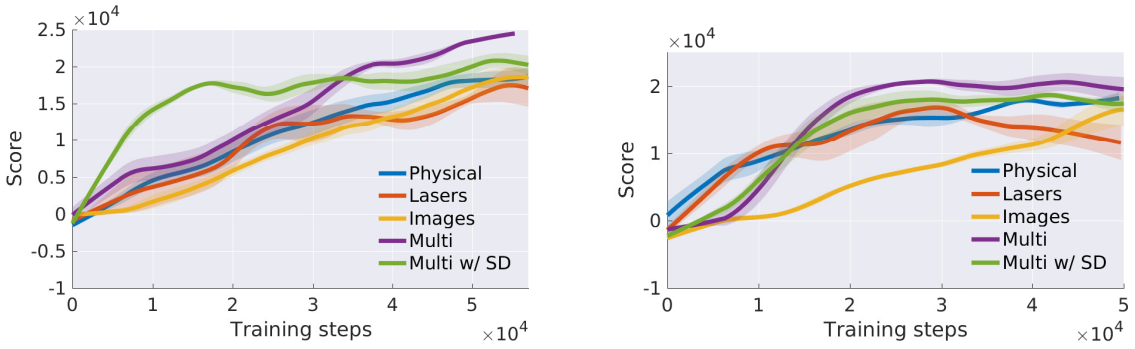

(a) NAF (b) DDPG

Figure 4.3: Training performance comparison of three baseline single sensor policies, and the proposed multimodal sensor policies, with and without Sensor Dropout.

the minibatch size of 16.

We used Adam [77] for learning the network parameters. For DDPG, the learning rates for actor and critic are 10^{-4} and 10^{-3}, respectively. We allow the actor and critic to maintain its own feature extraction module. In practice, sharing the same extraction module can lead to unstable training. Note that the NAF algorithm maintains three separate networks, which represent the value function ($V(s|\theta^V)$), policy network ($\mu(s|\theta^\mu)$), and the state-dependent covariance matrix in the action space ($P(s|\theta^L)$), respectively. To maintain a similar experiment setting and avoid unstable training, we maintain two independent feature extraction modules for θ^μ, and both θ^V and θ^L. In a similar vein, we apply a learning rate of 10^{-4} for θ^μ, and 10^{-3} for both θ^μ and θ^V.

4.2.2 Experimental Results

Training Summary

The training performance, for all the proposed models and their corresponding baselines, is shown in Fig. 4.3. The blue, red, and orange line represents three uni-modal policies. For DDPG, using high-dimensional sensory input directly impacts convergence rate of the policy. (Note that the *Images* uni-policy has a much larger dimensional state space compared with *Multi* policy.) Counter-intuitively, NAF performs a nearly linear improvement over training steps and is relatively insensitive to the dimensionality of the state space. However, adding Sensor Dropout

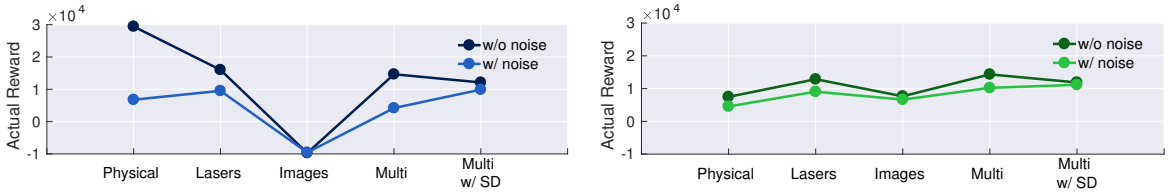

(a) NAF (b) DDPG

Figure 4.4: Policy Robustness Analysis: Darker lines connects average rewards of leaned policies with accurate sensing while the lighter lines connects the corresponding policies in the face of sensor noise.

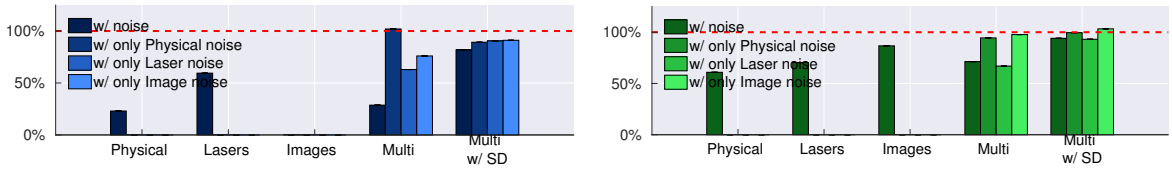

(a) NAF (b) DDPG

Figure 4.5: Policy Robustness Analysis: The bar box measures the relative scale among each of the models when noise is introduced. The red dotted lines show the performance without noise.

(SD) dramatically increases the convergence rate. Note that for both algorithms, the final performance for multimodal sensor policies trained with SD is slightly lower than training without SD, indicating that SD has a stochastic regularization effect like original Dropout.

Comparison with Baseline Models

Uni-modal policies: Note that, we assume perfect sensing during the training. However, to test performance in a more realistic scenario, we simulate mildly imperfect sensing by adding Gaussian noise. The perturbation sensitivity is compatible with a more standard Average Fisher Sensitivity (AFS) according to [78]. Policy performance with and without noise is plotted for comparison in Fig. 4.4 and 4.5. While Fig. 4.4 plots the actual reward performance, Fig. 4.5 summarizes the relative performance compared with a noiseless environment.

The performance of the NAF agent drops dramatically when the noise is introduced. We also observe that NAF in the multimodal is sensitive to states from sensors which are easily interpretable such as laser scanners. This effect shows that using an over-complete state representation holds a risk of the agent learning an undesired policy where the influence of different features gets unbalanced. The regularization introduced by Sensor Dropout alleviates this issue and learns a stable policy on both algorithms, with only a slight decrease of the performance compared with multimodal agents trained without SD. In summary, with the addition of noise, the performance drop is sometimes severe in a single input policy, as seen for NAF with physical state input. In comparison, the drop is almost negligible when Sensor Dropout is used.

Multiple Uni-modal Policy: Another intuitive baseline for the multi-sensor problem is to train each uni-modal sensor policy separately. Once individual policies are learned, we can train

Table 4.2: Performance of Policy

POLICY	W/O NOISE	W/ NOISE	PERFORMANCE DROP
MULTI UNI-MODAL W/ META CONTROLLER	1.51 ± 0.57	0.73 ± 0.40	51.7 %
MULTIMODAL W/ SD	2.54 ± 0.08	2.29 ± 0.60	9.8 %

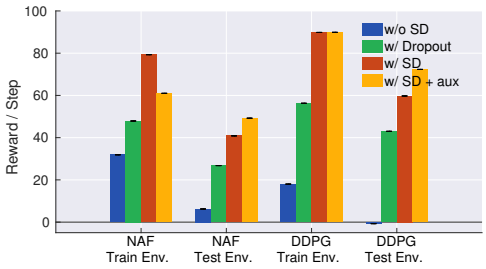

Figure 4.6: Policy performance when facing random sensor failure.

Table 4.3: Results of the sensitivity metric.

		TRAINING ENV.	TESTING ENV.
NAF	W/O SD	1.651	1.722
	W/ SD	**1.284**	**1.086**
DDPG	W/O SD	1.458	1.468
	W/ SD	**1.168**	**1.171**

an additional meta controller that select which policy to follow given the current state. For this, we take the best-trained policies of each sensor and train a meta-controller that takes the concatenated feature state from each sensor and output a $3DOF$ softmax layer as the probability of choosing each uni-modal sensor policy. The meta controller is trained under the standard policy gradient method, which can be found in [79] for more details.

Policy performance with and without noise for two approaches are summarized in Table 4.2. The performance of the baseline policy drops dramatically once noises are introduced, which implies that without any regularization the uni-modal policy is prone to over-fit. In fact, with the addition of noise, the performance drop is sometimes severe in physical-based or laser-based policy. In comparison, the policy trained with SD reaches a higher score in both scenarios, and the drop is almost negligible.

Policy Robustness Analysis

In this part, we further validate our hypothesis that SD reduces the learned policy's acute dependence on a subset of sensors in a multimodal setting. First, we consider a scenario when the system has detected malfunctions of sensors, and the agent needs to rely on the remaining sensors to make the decision. During testing, we randomly blocked off part of the sensor modules and scaled the rest of observation using the same rescaling mechanism as proposed in Section 4.1.2. Fig. 4.6 reports the average of the normalized reward of each model. A naive multimodal sensor policy without any stochastic regularization (blue bar) performs poorly in the face of partial sensor failure and transfer tasks. Adding original Dropout does make the policy more generalized, yet the performance is not comparable with SD or with SD and auxiliary loss. Interestingly, by reducing the variance of the multimodal sensor policy with auxiliary losses, policy tends to have a better generalization among other environments.

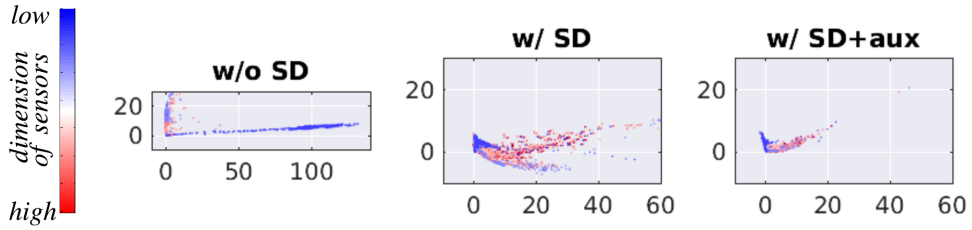

Figure 4.7: Two-dimensional PCA embedding of the representations in the last hidden layer assigned by the policy networks.

Policy Sensitivity Analysis

To further examine the impact of SD on effective sensor fusion, we monitor the extent to which the learned policy depends on each sensor block by measuring the gradient of the policy output w.r.t a subset block $\tilde{S}^{(i)}$. The technique is motivated from the salient map analysis [80], which has also been applied to DRL study recently [81]. To better analyze the effects of SD, we report on a the smaller subset by implementing SD layer to drop either (1) $(physical,\ laser)$ or (2) $vision$. Consequently, the *sensitivity* metric is formulated as the relative sensitivity of the policy on two sensor subsets. If the ratio increases, the agent's dependence shifts toward the sensor block in the numerator and vice versa. Assuming the fusion-of-interest is between the above-mentioned two subsets, we show in Table 4.3 that, using SD, the metric get closer to 1.0, indicating nearly equal importance to both the sensing modalities. The *sensitivity metric* is calculated as

$$\mathcal{T}_2^1 = \frac{1}{M}\sum_{i=1}^{M}\frac{\left|\nabla_{\tilde{S}_i^{(1)}}\mu(\tilde{S}|\theta^\mu)\Big|_{S_i}\right|}{\left|\nabla_{\tilde{S}_i^{(2)}}\mu(\tilde{S}|\theta^\mu)\Big|_{S_i}\right|} \tag{4.4}$$

Effect of Auxiliary Loss

In this experiment, we verify how the auxiliary loss helps reshape the multimodal sensor policy and reduce the action variance. We extract the representations of the last hidden layer assigned by the policy network throughout a fixed episode. At every time step, the representation induced by each sensor combination is collected. Our intuition is that the latent space represents how the policy network interprets the incoming sensor stream for reaction. Based on this assumption, an ideal multimodal sensor policy should map different sensor streams to a similar distribution as long as the information provided by each combination is representative to lead to the same output.

Fig. 4.7 shows the two-dimensional Principal Component Analysis (PCA) embedding on the latent space of each sub-policy. The blue dots correspond to the representations induced by the sub-policy that use high dimensional sensor (e.g. vision) as its input. On the other hand, the red dots represent the one with lower sensor stream such as odometry and range finder. Note that in practice, the covariance of the first third principal components contains around 85%. We provide

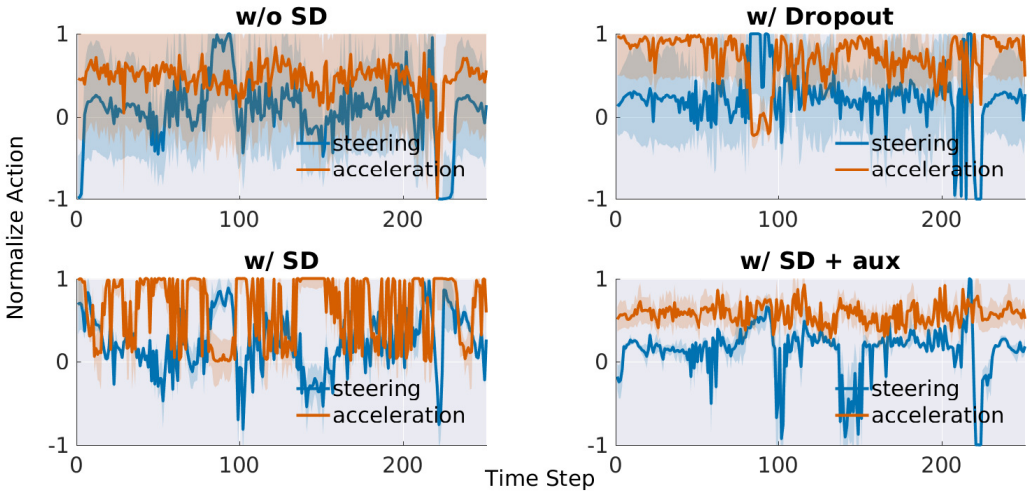

Figure 4.8: The variance of all the actions induced by sub-policy under each multimodal sensor policy. *Upper-left*: naive policy without any regularization. *Upper-right*: with standard Dropout. *Lower-left*: with Sensor Dropout. *Lower-right*: with Sensor Dropout and auxiliary loss.

the actual covariances for each component in the supplementary material.

As shown in Fig. 4.7, the naive multimodal sensor policy has a scattered distribution over the latent space, indicating that representative information from each sensor is treated very differently. In comparison, the policy trained with SD has a concentrated distribution, yet it is still distinguishable with respect to different sensors. Adding the auxiliary training loss encourages the true sensor fusion as the distribution becomes more integrated. During training, the policy is not only forced to make decisions under each sensor combination but also penalized with the disagreements among multimodal sensor policies. In fact, as shown in Fig. 4.8, the concentration of the latent space directly affects the action variance induced by each sub-policy. We provide the action variance value in the supplementary material.

4.3 Discussion

4.3.1 Full Sub-Policy Analysis

The performance of each sub-policy is summarized in Fig. 4.9. As shown in the first and third column, the performance of the naive multimodal sensor policy (red) and the policy trained with standard Dropout (blue) drop dramatically as the policies lose access to images, which share 87.9% of the total multimodal state. Though Dropout increases the performance of the policy in the testing environment, the generalization is limited to using the full multimodal state as input. On the other hand, Sensor Dropout (SD) generalize the policy across *sensor module* that make the sub-policies successfully transfer to the testing environment. It is worth mentioning that the policies trained with SD are capable of operating when both laser and image sensor are blocked.

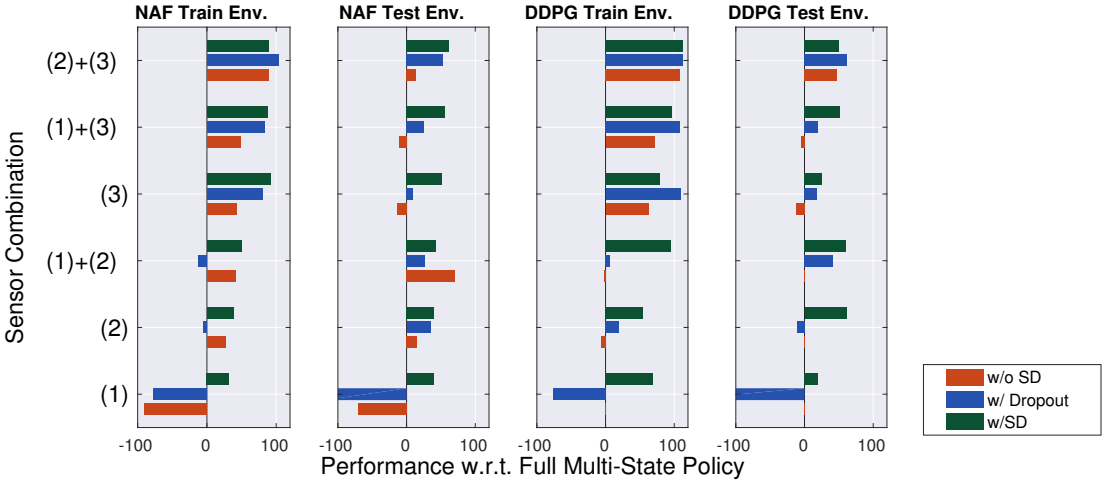

Figure 4.9: The full analysis of the performance of the total 6 sub-policies. The (1), (2), and (3) labels in y-axis represent physical state, laser, and image, respectively. The x-axis represents the remaining performance w.r.t. the SD policy with all sensor, *i.e.* (1)+(2)+(3).

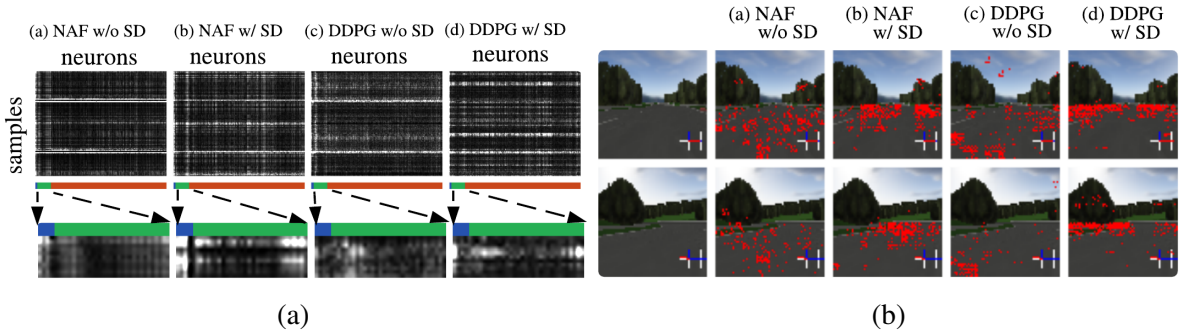

(a) (b)

Figure 4.10: (a)The visualization of the magnitude of gradient for each neuron. The whiter color means the higher gradient. The color bar represents three different sensor modules: physical state(blue), Laser(green), and Image(red). (b) The gradient responses of actions on the image input for each of the multimodal agents. The top 20% gradients are marked red.

4.3.2 Visualize Policy Attention Region

The average gradient in the policy sensitivity section can also be used to visualize the region among each sensor where the policy network pays attention. As shown in Fig. 4.10a, we observe that policies trained with SD have higher gradients on neurons corresponding to the corner inputs of the laser sensor, indicating that a more sparse and meaningful policy is learned. These corner inputs corresponded to the laser beams that are oriented perpendicularly to the vehicle's direction of motion, and give an estimate of its relative position on the track. To look for similar patterns, in Fig. 4.10b, image pixels with higher gradients are marked to visualize and interpret the policy's view of the world. We pick two scenarios, 1) straight track and 2) sharp left turn, depicted by the first and second rows in the figure. Note that though policies trained without SD tend to focus more on the road, those areas are in plain color and offer little salient information. In conclusion, policies trained with SD are more sensitive to features such as road boundary, which is crucial

Table 4.4: Covariance of the first three Principal Component

	NAF			DDPG		
PRINCIPAL COMPONENT	W/OSD	W/SD	W/SD+AUX	W/OSD	W/SD	W/SD+AUX
FIRST (%)	94.9	82.0	58.9	93.4	59.2	47.4
SECOND (%)	4.1	12.3	25.2	3.1	20.7	21.9
THIRD (%)	0.6	3.1	5.3	1.6	6.2	6.1

Table 4.5: Action Variation w.r.t. multimodal sensor

	NAF			DDPG		
	W/OSD	W/SD	W/SD+AUX	W/OSD	W/SD	W/SD+AUX
STEERING	0.1177	0.0819	**0.0135**	0.3329	0.0302	**0.0290**
ACCELERATION	0.4559	0.0472	**0.0186**	0.5714	0.0427	**0.0143**

for long horizon planning. In comparison, networks trained without SD have relatively low and unclear gradients over both laser and image sensor state space.

4.4 Supplementary Material

The covariance of PCA and the actual action variance is summarized in Table 4.4 and 4.5, respectively.

Chapter 5

Learning from Demonstration using DIRL

Most of the robotics problems can be solved under optimization framework. For the motion planning problem, the objective is to find a sequence of control actions that minimizes the accumulated costs toward the goal state. Reinforcement learning, on the other hand, formulates the problem as finding a policy that maximizes the expected accumulated rewards collected from the environment. Both problems require a definition of the cost/reward function of the interested robotics tasks. However, unlike in the urban environment where cost function can be well defined in a rule-based structure, finding a cost function for off-road navigation can be non-trivial and often requires lots of handy tunings [41]. Here, motivated by the recent successes [42, 43] to using deep neural nets to approximate the cost functions, we implement a similar algorithm for the off-road application.

5.1 Proposed Methods

The pipeline of deep inverse reinforcement learning (DIRL) is shown in Fig. 5.1. The raw sensor inputs first process through the feature extraction module. The resulting feature maps are used as the input of the cost function that is approximated by a deep neural network. Once the cost map is generated, we can formulate the corresponding Markov Decision Process (MDP) problem and solve for the expected state-visited frequencies (SVF). Finally, the gradient is applied using Eq. 2.14 by comparing the expected SVF inferred under the current reward structure with the target SVF calculated from the demonstrations.

5.1.1 Learning from Failure for DIRL

The fundamental challenge arises with DIRL is the spatially sparse gradient feedback. Since the gradient signals only come from the difference between demonstrations and expected trajectories, the loss feedbacks in training will inevitably focus more on the traversable regions. The problem can be alleviated by pre-training the network under standard image segmentation framework [82], which provide pixel-wise feedbacks for error terms. Here, we propose an alternative approach that re-formulated the same problem with *negative* demonstrations.

Following the same convention in Section 2.4, we now denote the positive and negative

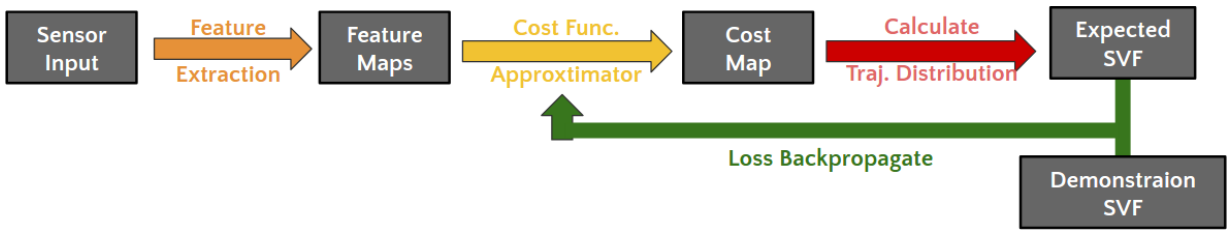

Figure 5.1: Block diagram of deep inverse reinforcement learning.

demonstrations as D_{pos} and D_{neg}, respectively. The log likelihood (Eq. 2.12) can be reformulated as:

$$L(\theta) = \log P(D_{pos}, D_{neg}, \theta | r) \tag{5.1}$$
$$= \log P(D_{pos}|r) + \log P(D_{neg}|r^{-1}) + \log P(\theta) \tag{5.2}$$

With the L2-regularization, the new gradient becomes:

$$\frac{\partial L}{\partial \theta} = \left(\mu_{D_{pos}} - \mathbb{E}_r[\mu]\right) \frac{\partial r}{\partial \theta} + \left(\mu_{D_{neg}} - \mathbb{E}_{r^{-1}}[\mu]\right) \frac{\partial r^{-1}}{\partial r} \frac{\partial r}{\partial \theta} + \frac{\lambda}{2}\|\theta\|^2 \tag{5.3}$$
$$= \left(\mu_{D_{pos}} - \mathbb{E}_r[\mu] + \mathbb{E}_{r^{-1}}[\mu] - \mu_{D_{neg}}\right) \cdot \frac{\partial r}{\partial \theta} + \frac{\lambda}{2}\|\theta\|^2 \tag{5.4}$$

where $r^{-1} = constant - r$ stands for the *inverted* reward map. By jointly optimizing with the negative demonstrations, we can increase the gradient feedbacks for non-traversable regions where the positive demonstrations will never capture.

5.1.2 Modeling Optimality Ambiguity

As described in Section 2.4, the objective function of IRL is usually formulated either in a fashion of structured support vector machines (SSVMs), or conditional random fields (CRFs). While Maximum Margin Planning (MMP) falls in the first category, Maximum Entropy IRL (ME-IRL) can represent the second category. However, both categories share a similar form of the gradient of its objective. Recall Eq. 2.9 and Eq. 2.14, while gradient of MMP involves in solving the *optimal* trajectory on the evolving reward map, the gradient of ME-IRL instead requires solving the *expectation* of the trajectory distribution. The rest calculations remain mostly the same. Pletscher et al. [83] proposed a generalized loss that models the observed expert behaviors with Gibbs distribution and an inverse temperature $\beta \in \mathbb{R}^+$.

$$P_\beta(\xi_i|r_\theta) = \frac{1}{Z_\beta} \exp\left(\beta r_\theta(\xi_i)\right) \tag{5.5}$$

$$\text{,where} \quad Z_\beta = \sum_{\xi \in \Xi} \exp\left(\beta r_\theta(\xi)\right) \text{ is the normalization constant.} \tag{5.6}$$

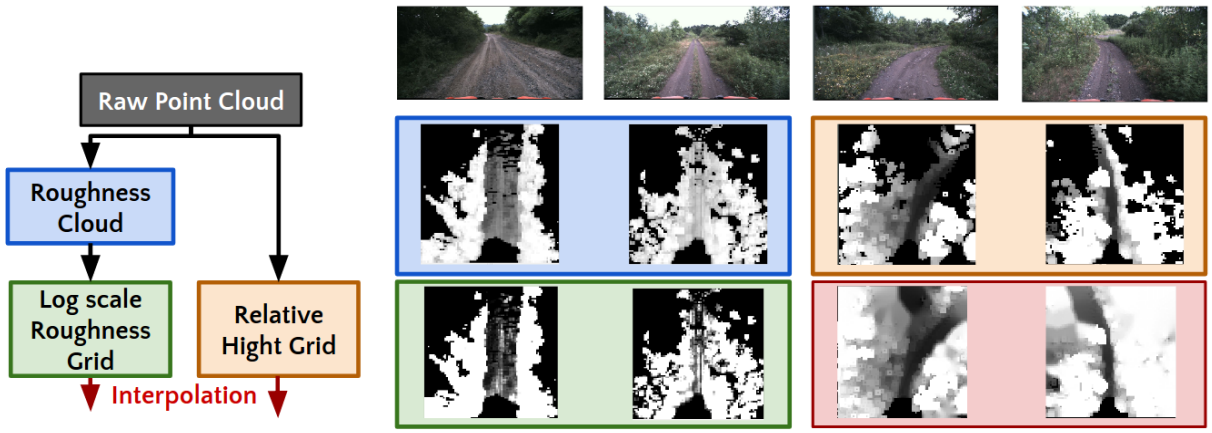

Figure 5.2: The extracted feature maps from LiDAR. The flow chart is shown on the left of the figure, while examples of the actual collected data on field are shown on the right of the figure.

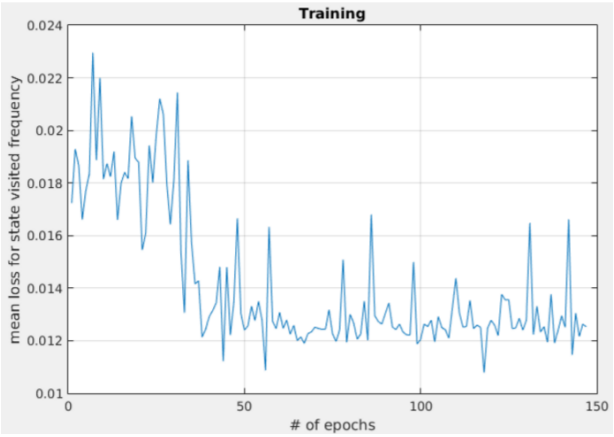

Figure 5.3: Training curve of DIRL in Gascola dataset.

As β increases, the exponent term dominates, and the corresponding distribution becomes sharper. If $\beta \to \infty$, the distribution degenerates to solving the $\arg\max$, *i.e.* the optimal trajectory $P(\xi_i|r_\theta) = \mathbb{1}\left\{\xi_i = \text{argmax}_{\xi \in \Xi} r_\theta(\xi)\right\}$. On the other hand, if $\beta \to 1$, the distribution becomes the same form of the one used in ME-IRL. In other words, the SSVM-like and CRF-like losses are framed under the same framework and can be seen as two special cases located at the opposite side of the spectrum. $\beta \to 0 P(\xi_i|r_\theta) = uniform$

This generalized loss introduces a new parameter β that captures on which level of the *optimality* is presented by the demonstration trajectories. By integrating this generalized loss in our computational graph, the parameter can be optimized jointly during training.

5.2 Experiments Results

Following the similar setup in Chapter 3, we use Yamaha Viking VI side-by-side ATV as our main testing platform, with LiDAR as our primary input sensor. For off-road navigation where

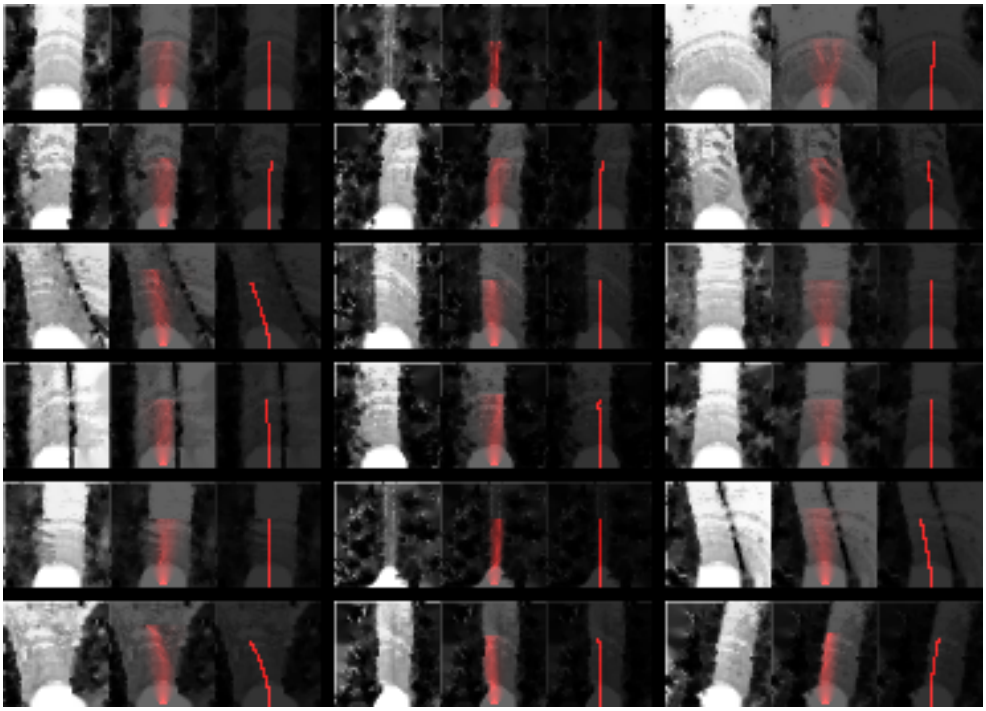

Figure 5.4: Final cost map on testing set. The left, middle, and right image represent the output cost map, the same cost map overlapped with expected SVF, and with demonstrations, respectively.

scenes can change dramatically, LiDAR provides a more reliable measurement for the safety concern. In addition, informative features such as terrain roughness can be inferred straightforwardly. We collect the dataset with total 150 human demonstrations covering an off-road testing field at Gascola, PA. Each sample covers the $20m \times 20m$ region in the front of the ATV. Since the Gascola dataset is relatively small, we use a shallow multilayer perception as the cost function.

The first feature map captures information about terrain roughness. As shown in Fig. 5.2, the basic approach to infer terrain roughness from the raw point cloud is to first divide it into patches. For each patch, a normal plane is fitted using standard least square regression. Once the plane parameters are calculated, the *roughness index* can be inferred by averaging plane variances within each patch. However, this naive roughness index is sensitive to hyper-parameter such as patch size and rescaling factors. In off-road environments where terrain types can vary a lot, this approach can fail to extract reasonable features when trails become narrow, as shown in the second column of Fig. 5.2. To alleviate this issue, we replace the original roughness index with the log-scale value. The log scale helps amplify the slight difference among traversable terrains in which we have more interests. On the other hand, the roughness difference among the non-traversable terrain such as bush or trees is flattened under the log scale. Another informative feature map is the relative height with respect to the vehicle standing level.

The intuition behind the two feature maps is that the vehicle should prefer driving over terrain that is smoother or at the similar horizontal level of its current local frame. Note that both feature

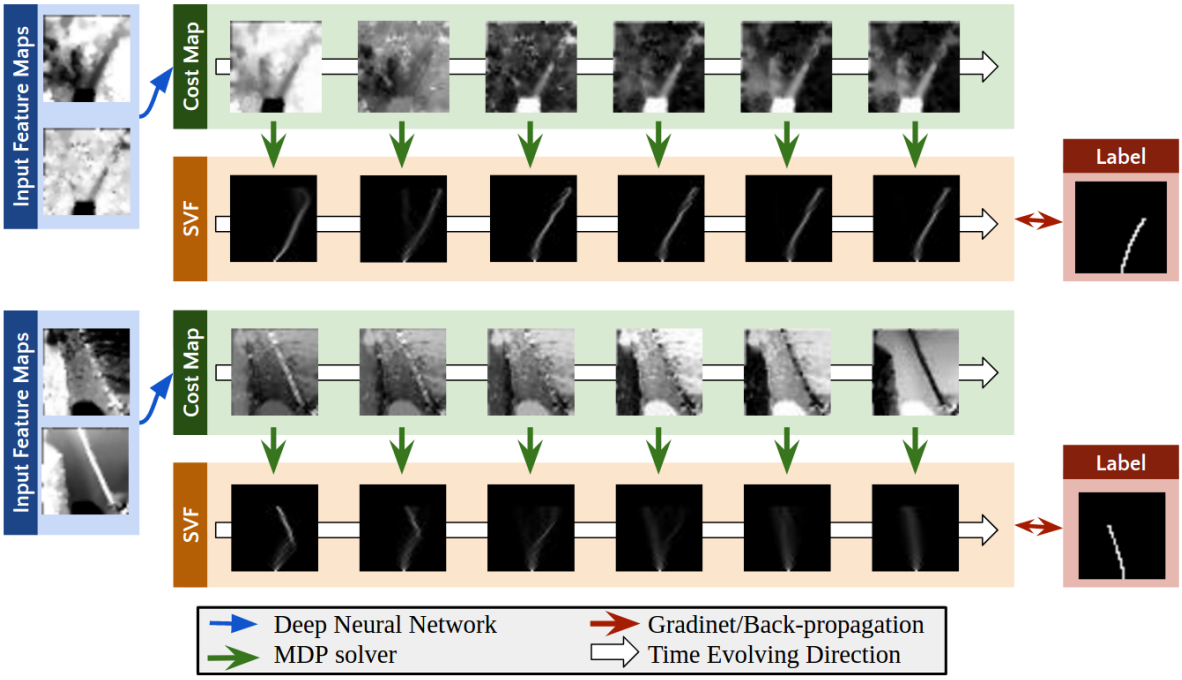

Figure 5.5: Samples of intermediate cost maps during training.

maps are projected on a top-down view, leaving some parts of the feature maps unoccupied. However, the invisible grids may confuse the network and make the framework fragile to the senses. Though the problem can be alleviated by simply providing an additional feature map that specifies the visibility, it usually requires much more data and the use of convolution layer [42, 43]. Since our dataset is relatively small, we alleviate this issue with an alternative approach. Instead, we apply a standard image inpainting technique [84] that effectively helps infer the invisible region given the geometric shape of the visible trails. The feature maps before and after the interpolation are shown in the orange and red area in Fig. 5.2, respectively.

The training curve is summarized in Fig. 5.3, with the resulting cost maps on testing data set shown in Fig. 5.4. The training curve converges within 55 episodes in our Gascola data set, yet the testing result shows its efficacy by capturing untraversable region like fences and distinguishing the nuance of terrain roughness on both wide and narrow trails. Fig. 5.5 visualizes the intermediate cost maps of two samples during training, with the first and second row represent the intersection of a narrow trail, and a wider trail beside a fence, respectively.

Chapter 6

Conclusion and Future Work

This thesis investigates the application of both traditional motion planning and end-to-end learning algorithms in the off-road settings. We first start with a more traditional method by proposing an RRT-based local planner for high-speed maneuvering on a full-size all-terrain vehicle (ATV). The local planner utilizes a data-driven vehicle model for roll-out in high dimensional state space. Several modifications are implemented to efficiently solve for the minimal traveling-time trajectory. A simplified version of occupancy grid is built in the global frame, with the obstacle detection module implemented with height map algorithm. Results from field experiments show that the proposed planner can successfully avoid obstacles on a turnpike with vehicle velocity up to the maximum operating speed.

Alternatively, we propose an end-to-end controller that uses multi-sensor input to learn an autonomous navigation policy in a physics-based car racing simulator. To make the learning problem representative of the real-world setting, we use a sensor set including a front-view camera with RGB channel, laser scan, and physical states such as odometry. We introduce a new stochastic regularization technique called Sensor Dropout to promote an effective fusing of information from multiple sensors. The variance of the resulting policy can be further reduced by introducing an auxiliary loss during training. We show that the aid of Sensor Dropout reduces the policy sensitivity to a particular sensor subset, and makes it capable of functioning even in the face of partial sensor failure. Moreover, through the visualization of gradients, we show that the learned policies are conditioned on the same latent distribution despite having multiple sensory observations spaces - a hallmark of true sensor-fusion.

Lastly, we investigate into the deep inverse reinforcement learning (DIRL) algorithms that infer the cost, or traversability, of the unstructured terrain by leveraging a large volume of human demonstration data collected on the field. We propose two slight modifications to overcome issues that arise from DIRL training, such as sparse gradients, and ambiguity of the demonstration optimality. This framework is tested on a full-size ATV in the off-road environment.

Some interesting directions that merit further study include:

1. Construct a more complex vehicle model in 3D space for the model-based local planner, strengthen the collision map with more informative data such as mesh, or segmentation, and planner optimization with RRT tree maintenance.
2. Extend the end-to-end framework to other environments such as real robotics systems, and

other algorithms like GPS[85], TRPO [47], and Q-Prop [72], etc. Secondly, systematic investigation into problems such as how to augment the reward function for other important driving tasks like collision avoidance, and lane changing, and how to adaptively adjust the SD distribution during training.

3. Increase the model complexity of DIRL framework to handle richer terrain textures, use continuous state IRL approaches like RE-IRL [86] and path integral [87] to better handle vehicle constraints under extreme conditions like the sharp turning at intersections.

Bibliography

[1] Chris Urmson, Joshua Anhalt, Drew Bagnell, Christopher Baker, Robert Bittner, MN Clark, John Dolan, Dave Duggins, Tugrul Galatali, Chris Geyer, et al. Autonomous driving in urban environments: Boss and the urban challenge. *Journal of Field Robotics*, 25(8):425–466, 2008. (document), 1.1, 1.1

[2] Anthony Stentz, John Bares, Thomas Pilarski, and David Stager. The crusher system for autonomous navigation. *AUVSIs Unmanned Systems North America*, 3, 2007. (document), 1.1, 1.1.1

[3] Mariusz Bojarski, Davide Del Testa, Daniel Dworakowski, Bernhard Firner, Beat Flepp, Prasoon Goyal, Lawrence D Jackel, Mathew Monfort, Urs Muller, Jiakai Zhang, et al. End to end learning for self-driving cars. *arXiv preprint arXiv:1604.07316*, 2016. (document), 1.1.2, 1.2

[4] Shixiang Gu, Ethan Holly, Timothy Lillicrap, and Sergey Levine. Deep reinforcement learning for robotic manipulation with asynchronous off-policy updates. *arXiv preprint arXiv:1610.00633*, 2016. (document), 1.3

[5] Preferred Network LLC. Autonomous robot car control demonstration in ces2016, 2016. URL `https://www.youtube.com/watch?v=7A9UwxvgcV0`. (document), 1.3

[6] Michael Bode. Learning the forward predictive model for an off-road skid-steer vehicle. 2007. (document), 3.1

[7] Wikipedia. Motion plannning — Wikipedia, the free encyclopedia, 2017. URL `https://en.wikipedia.org/w/index.php?title=Motion_planning&oldid=771978059`. [Online; accessed 24-March-2017]. 1.1

[8] Chris Urmson, J Andrew Bagnell, Christopher R Baker, Martial Hebert, Alonzo Kelly, Raj Rajkumar, Paul E Rybski, Sebastian Scherer, Reid Simmons, Sanjiv Singh, et al. Tartan racing: A multi-modal approach to the darpa urban challenge. 2007. 1.1, 1.1.2

[9] Grady Williams, Nolan Wagener, Brian Goldfain, Paul Drews, James M Rehg, Byron Boots, and Evangelos A Theodorou. Information theoretic mpc for model-based reinforcement learning. In *Robotics and Automation, 2017. ICRA 2017. Proceedings 2017 IEEE International Conference on*, 2017. 1.1

[10] J Zico Kolter, Christian Plagemann, David T Jackson, Andrew Y Ng, and Sebastian Thrun. A probabilistic approach to mixed open-loop and closed-loop control, with application to extreme autonomous driving. In *Robotics and Automation (ICRA), 2010 IEEE International Conference on*, pages 839–845. IEEE, 2010. 1.1

[11] Grady Williams, Paul Drews, Brian Goldfain, James M Rehg, and Evangelos A Theodorou. Aggressive driving with model predictive path integral control. In *Robotics and Automation (ICRA), 2016 IEEE International Conference on*, pages 1433–1440. IEEE, 2016. 1.1

[12] Andrew Gray, Yiqi Gao, Theresa Lin, J Karl Hedrick, H Eric Tseng, and Francesco Borrelli. Predictive control for agile semi-autonomous ground vehicles using motion primitives. In *American Control Conference (ACC), 2012*, pages 4239–4244. IEEE, 2012. 1.1

[13] Mark Cutler and Jonathan P How. Autonomous drifting using simulation-aided reinforcement learning. In *Robotics and Automation (ICRA), 2016 IEEE International Conference on*, pages 5442–5448. IEEE, 2016. 1.1

[14] Mark Cutler, Thomas J Walsh, and Jonathan P How. Reinforcement learning with multi-fidelity simulators. In *Robotics and Automation (ICRA), 2014 IEEE International Conference on*, pages 3888–3895. IEEE, 2014. 1.1

[15] Sven Koenig and Maxim Likhachev. Dˆ* lite. 1.1.1

[16] Yoshiaki Kuwata, Gaston A Fiore, Justin Teo, Emilio Frazzoli, and Jonathan P How. Motion planning for urban driving using rrt. In *Intelligent Robots and Systems, 2008. IROS 2008. IEEE/RSJ International Conference on*, pages 1681–1686. IEEE, 2008. 1.1.1

[17] Alonzo Kelly, Anthony Stentz, Omead Amidi, Mike Bode, David Bradley, Antonio Diaz-Calderon, Mike Happold, Herman Herman, Robert Mandelbaum, Tom Pilarski, et al. Toward reliable off road autonomous vehicles operating in challenging environments. *The International Journal of Robotics Research*, 25(5-6):449–483, 2006. 1.1.1

[18] Dmitri Dolgov, Sebastian Thrun, Michael Montemerlo, and James Diebel. Practical search techniques in path planning for autonomous driving. *Ann Arbor*, 1001:48105, 2008. 1.1.1

[19] H Shibly, Karl Iagnemma, and S Dubowsky. An equivalent soil mechanics formulation for rigid wheels in deformable terrain, with application to planetary exploration rovers. *Journal of terramechanics*, 42(1):1–13, 2005. 1.1.1

[20] D Rubinstein and R Hitron. A detailed multi-body model for dynamic simulation of off-road tracked vehicles. *Journal of Terramechanics*, 41(2):163–173, 2004. 1.1.1

[21] James J Kuffner and Steven M LaValle. Rrt-connect: An efficient approach to single-query path planning. In *Robotics and Automation, 2000. Proceedings. ICRA'00. IEEE International Conference on*, volume 2, pages 995–1001. IEEE, 2000. 1.1.1, 1, 3, 3.1

[22] Jeong hwan Jeon, Sertac Karaman, and Emilio Frazzoli. Anytime computation of time-optimal off-road vehicle maneuvers using the rrt. In *Decision and Control and European Control Conference (CDC-ECC), 2011 50th IEEE Conference on*, pages 3276–3282. IEEE, 2011. 1.1.1, 3.2.2

[23] Chenyi Chen, Ari Seff, Alain Kornhauser, and Jianxiong Xiao. Deepdriving: Learning affordance for direct perception in autonomous driving. In *Proceedings of the IEEE International Conference on Computer Vision*, pages 2722–2730, 2015. 1.1.2

[24] Huazhe Xu, Yang Gao, Fisher Yu, and Trevor Darrell. End-to-end learning of driving models from large-scale video datasets. In *Proceedings of the IEEE Conference on Com-*

puter Vision and Pattern Recognition, 2017. 1.1.2

[25] Stéphane Ross, Geoffrey J Gordon, and Drew Bagnell. A reduction of imitation learning and structured prediction to no-regret online learning. In *AISTATS*, volume 1, page 6, 2011. 1.1.2

[26] Volodymyr Mnih, Koray Kavukcuoglu, David Silver, Alex Graves, Ioannis Antonoglou, Daan Wierstra, and Martin Riedmiller. Playing atari with deep reinforcement learning. In *NIPS'13 Workshop on Deep Learning*, 2013. 1.1.2, 2.2, 2.2.1

[27] Volodymyr Mnih, Koray Kavukcuoglu, David Silver, Andrei A Rusu, Joel Veness, Marc G Bellemare, Alex Graves, Martin Riedmiller, Andreas K Fidjeland, Georg Ostrovski, et al. Human-level control through deep reinforcement learning. *Nature*, 518(7540):529–533, 2015. 1.1.2, 2.2.1, 2.2.1

[28] Xue Bin Peng, Glen Berseth, and Michiel van de Panne. Terrain-adaptive locomotion skills using deep reinforcement learning. *ACM Transactions on Graphics (Proc. SIGGRAPH 2016)*, 35(4), 2016. 1.1.2

[29] Craig Quiter. Deepdrive: self-driving car ai, 2016. URL `http://deepdrive.io/`. 1.1.2

[30] Udacity. Udacity's self-driving car simulator. `https://github.com/udacity/self-driving-car-sim`, 2017. 1.1.2

[31] Ziyan Wang Cewu Lu Yurong You, Xinlei Pan. Virtual to real reinforcement learning for autonomous driving. *arXiv preprint arXiv:1704.03952*, 2017. 1.1.2

[32] Ahmed Hussain Qureshi, Yutaka Nakamura, Yuichiro Yoshikawa, and Hiroshi Ishiguro. Robot gains social intelligence through multimodal deep reinforcement learning. In *Humanoid Robots (Humanoids), 2016 IEEE-RAS 16th International Conference on*, pages 745–751. IEEE, 2016. 1.1.2

[33] Sergey Levine, Chelsea Finn, Trevor Darrell, and Pieter Abbeel. End-to-end training of deep visuomotor policies. *Journal of Machine Learning Research*, 17(39):1–40, 2016. 1.1.2

[34] Piotr Mirowski, Razvan Pascanu, Fabio Viola, Hubert Soyer, Andy Ballard, Andrea Banino, Misha Denil, Ross Goroshin, Laurent Sifre, Koray Kavukcuoglu, Dharshan Kumaran, and Raia Hadsell. Learning to navigate in complex environments. In *International Conference on Learning Representations (ICLR)*, 2017. 1.1.2, 4.1.3

[35] Jos Elfring, Rein Appeldoorn, and Maurice Kwakkernaat. Multisensor simultaneous vehicle tracking and shape estimation. In *Intelligent Vehicles Symposium (IV), 2016 IEEE*, pages 630–635. IEEE, 2016. 1.1.2

[36] Hyunggi Cho, Young-Woo Seo, BVK Vijaya Kumar, and Ragunathan Raj Rajkumar. A multi-sensor fusion system for moving object detection and tracking in urban driving environments. In *Robotics and Automation (ICRA), 2014 IEEE International Conference on*, pages 1836–1843. IEEE, 2014. 1.1.2

[37] Michael Darms, Paul Rybski, and Chris Urmson. Classification and tracking of dynamic objects with multiple sensors for autonomous driving in urban environments. In *Intelligent*

Vehicles Symposium, 2008 IEEE, pages 1197–1202. IEEE, 2008. 1.1.2

[38] Bernhard Wymann, E Espié, C Guionneau, C Dimitrakakis, R Coulom, and A Sumner. Torcs, the open racing car simulator. *Software available at http://torcs. sourceforge. net*, 2000. 1.2, 2, 4, 4.2.1

[39] Shixiang Gu, Timothy Lillicrap, Ilya Sutskever, and Sergey Levine. Continuous deep q-learning with model-based acceleration. In *Proceedings of The 33rd International Conference on Machine Learning*, pages 2829–2838, 2016. 1.2, 2.2, 2.2.1, 4

[40] Timothy P. Lillicrap, Jonathan J. Hunt, Alexander Pritzel, Nicolas Heess, Tom Erez, Yuval Tassa, David Silver, and Daan Wierstra. Continuous control with deep reinforcement learning. In *International Conference on Learning Representations (ICLR)*, 2016. 1.2, 2.2, 2.2.1, 4, 4.2.1

[41] David Silver, J Andrew Bagnell, and Anthony Stentz. Learning from demonstration for autonomous navigation in complex unstructured terrain. *The International Journal of Robotics Research*, 29(12):1565–1592, 2010. 1.2, 5

[42] Markus Wulfmeier, Peter Ondruska, and Ingmar Posner. Maximum entropy deep inverse reinforcement learning. *arXiv preprint arXiv:1507.04888*, 2015. 1.2, 3, 2.4, 5, 5.2

[43] Markus Wulfmeier, Dominic Zeng Wang, and Ingmar Posner. Watch this: Scalable cost-function learning for path planning in urban environments. In *Intelligent Robots and Systems (IROS), 2016 IEEE/RSJ International Conference on*, pages 2089–2095. IEEE, 2016. 1.2, 2.4, 5, 5.2

[44] Steven M LaValle. Rapidly-exploring random trees: A new tool for path planning. 1998. 2.1

[45] Sertac Karaman and Emilio Frazzoli. Sampling-based algorithms for optimal motion planning. *The international journal of robotics research*, 30(7):846–894, 2011. 2.1

[46] Volodymyr Mnih, Adria Puigdomenech Badia, Mehdi Mirza, Alex Graves, Timothy P Lillicrap, Tim Harley, David Silver, and Koray Kavukcuoglu. Asynchronous methods for deep reinforcement learning. In *International Conference on Machine Learning*, 2016. 2.2, 4.2.1

[47] John Schulman, Sergey Levine, Pieter Abbeel, Michael I Jordan, and Philipp Moritz. Trust region policy optimization. In *ICML*, pages 1889–1897, 2015. 2.2, 2

[48] Richard S Sutton, David A McAllester, Satinder P Singh, Yishay Mansour, et al. Policy gradient methods for reinforcement learning with function approximation. In *NIPS*, volume 99, pages 1057–1063, 1999. 2.2.1

[49] David Silver, Guy Lever, Nicolas Heess, Thomas Degris, Daan Wierstra, and Martin Riedmiller. Deterministic policy gradient algorithms. In *ICML*, 2014. 2.2.1

[50] George E Uhlenbeck and Leonard S Ornstein. On the theory of the brownian motion. *Physical review*, 36(5):823, 1930. 2.2.1, 4.2.1

[51] Nitish Srivastava, Geoffrey E Hinton, Alex Krizhevsky, Ilya Sutskever, and Ruslan Salakhutdinov. Dropout: a simple way to prevent neural networks from overfitting. *Journal of Machine Learning Research*, 15(1):1929–1958, 2014. 2.3, 4.1.2

[52] Calvin Murdock, Zhen Li, Howard Zhou, and Tom Duerig. Blockout: Dynamic model selection for hierarchical deep networks. In *Proceedings of the IEEE Conference on Computer Vision and Pattern Recognition*, pages 2583–2591, 2016. 2.3

[53] Li Wan, Matthew Zeiler, Sixin Zhang, Yann L Cun, and Rob Fergus. Regularization of neural networks using dropconnect. In *Proceedings of the 30th International Conference on Machine Learning (ICML-13)*, pages 1058–1066, 2013. 2.3

[54] David Krueger, Tegan Maharaj, János Kramár, Mohammad Pezeshki, Nicolas Ballas, Nan Rosemary Ke, Anirudh Goyal, Yoshua Bengio, Hugo Larochelle, Aaron Courville, et al. Zoneout: Regularizing rnns by randomly preserving hidden activations. *arXiv preprint arXiv:1606.01305*, 2016. 2.3

[55] Natalia Neverova, Christian Wolf, Graham Taylor, and Florian Nebout. Moddrop: adaptive multi-modal gesture recognition. *IEEE Transactions on Pattern Analysis and Machine Intelligence*, 38(8):1692–1706, 2016. 2.3

[56] Fan Li, Natalia Neverova, Christian Wolf, and Graham Taylor. Modout: Learning to fuse modalities via stochastic regularization. *Journal of Computational Vision and Imaging Systems*, 2(1), 2016. 2.3

[57] Andrew Y Ng, Stuart J Russell, et al. Algorithms for inverse reinforcement learning. 2.4

[58] Pieter Abbeel and Andrew Y Ng. Apprenticeship learning via inverse reinforcement learning. In *Proceedings of the twenty-first international conference on Machine learning*, page 1. ACM, 2004. 2.4, 2.4

[59] Nathan D Ratliff, J Andrew Bagnell, and Martin A Zinkevich. Maximum margin planning. In *Proceedings of the 23rd international conference on Machine learning*, pages 729–736. ACM, 2006. 2.4

[60] Brian D Ziebart, Andrew L Maas, J Andrew Bagnell, and Anind K Dey. Maximum entropy inverse reinforcement learning. In *AAAI*, volume 8, pages 1433–1438. Chicago, IL, USA, 2008. 2.4

[61] Alonzo Kelly, Thomas Howard, and Colin Green. Terrain aware inversion of predictive models for high-performance ugvs. In *Defense and Security Symposium*, pages 65611R–65611R. International Society for Optics and Photonics, 2007. 3.1

[62] Thomas Howard and Alonzo Kelly. Trajectory generation on rough terrain considering actuator dynamics. In *Field and service robotics*, pages 479–490. Springer, 2006. 3.1

[63] Thomas M Howard and Alonzo Kelly. Terrain-adaptive generation of optimal continuous trajectories for mobile robots. 3.1

[64] David Wettergreen and Michael Wagner. Developing a framework for reliable autonomous surface mobility. 2012. 3.2.1

[65] Martin A Fischler and Robert C Bolles. Random sample consensus: a paradigm for model fitting with applications to image analysis and automated cartography. *Communications of the ACM*, 24(6):381–395, 1981. 3.2.1

[66] Andrew M Ladd and Lydia E Kavraki. Motion planning in the presence of drift, underactuation and discrete system changes. In *Robotics: Science and Systems*, pages 233–240,

2005. 3.1

[67] David Hsu, J-C Latombe, and Rajeev Motwani. Path planning in expansive configuration spaces. In *Robotics and Automation, 1997. Proceedings., 1997 IEEE International Conference on*, volume 3, pages 2719–2726. IEEE, 1997. 3.1

[68] Ioan A Şucan and Lydia E Kavraki. Kinodynamic motion planning by interior-exterior cell exploration. In *Algorithmic Foundation of Robotics VIII*, pages 449–464. Springer, 2009. 3.1

[69] Ioan A. Şucan, Mark Moll, and Lydia E. Kavraki. The Open Motion Planning Library. *IEEE Robotics & Automation Magazine*, 19(4):72–82, December 2012. doi: 10.1109/MRA.2012.2205651. `http://ompl.kavrakilab.org`. 3.2.2

[70] Dave Ferguson, Nidhi Kalra, and Anthony Stentz. Replanning with rrts. In *Robotics and Automation, 2006. ICRA 2006. Proceedings 2006 IEEE International Conference on*, pages 1243–1248. IEEE, 2006. 3.2.2

[71] Ratan Hudda, Clint Kelly, Garrett Long, Jun Luo, Atul Pandit, Dave Phillips, Lubab Sheet, and Ikhlaq Sidhu. Self driving cars. 2013. 4.1

[72] Shixiang Gu, Timothy P. Lillicrap, Zoubin Ghahramani, Richard E. Turner, and Sergey Levine. Q-prop: Sample-efficient policy gradient with an off-policy critic. In *International Conference on Learning Representations (ICLR)*, 2017. 4.1.3, 2

[73] Guillaume Lample and Devendra Singh Chaplot. Playing fps games with deep reinforcement learning. *arXiv preprint arXiv:1609.05521*, 2016. 4.1.3

[74] Alexey Dosovitskiy and Vladlen Koltun. Learning to act by predicting the future. In *International Conference on Learning Representations (ICLR)*, 2017. 4.1.3

[75] Naoto Yoshida. Gym-torcs. `https://github.com/ugo-nama-kun/gym_torcs`, 2016. 4.2.1

[76] Yan-Pan Lau. Using keras and deep deterministic policy gradient to play torcs. `https://yanpanlau.github.io/2016/10/11/Torcs-Keras.html`, 2016. 4.2.1

[77] Diederik P Kingma and Jimmy Lei Ba. Adam: A method for stochastic optimization. 2015. 4.2.1

[78] Andrei A Rusu, Neil C Rabinowitz, Guillaume Desjardins, Hubert Soyer, James Kirkpatrick, Koray Kavukcuoglu, Razvan Pascanu, and Raia Hadsell. Progressive neural networks. *arXiv preprint arXiv:1606.04671*, 2016. 4.2.2

[79] Richard Liaw, Sanjay Krishnan, Animesh Garg, Daniel Crankshaw, Joseph E Gonzalez, and Ken Goldberg. Composing meta-policies for autonomous driving using hierarchical deep reinforcement learning. 2017. 4.2.2

[80] Karen Simonyan, Andrea Vedaldi, and Andrew Zisserman. Deep inside convolutional networks: Visualising image classification models and saliency maps. In *Proceedings of the IEEE Conference on Computer Vision and Pattern Recognition*, 2014. 4.2.2

[81] Ziyu Wang, Nando de Freitas, and Marc Lanctot. Dueling network architectures for deep reinforcement learning. In *international Conference on Machine Learning (ICML)*, 2016.

4.2.2

[82] Markus Wulfmeier, Dushyant Rao, and Ingmar Posner. Incorporating human domain knowledge into large scale cost function learning. 2016. 5.1.1

[83] Patrick Pletscher, Cheng Soon Ong, and Joachim M Buhmann. Entropy and margin maximization for structured output learning. In *Joint European Conference on Machine Learning and Knowledge Discovery in Databases*, pages 83–98. Springer, 2010. 5.1.2

[84] Alexandru Telea. An image inpainting technique based on the fast marching method. *Journal of graphics tools*, 9(1):23–34, 2004. 5.2

[85] Sergey Levine and Vladlen Koltun. Guided policy search. In *International Conference on Machine Learning (ICML)*, pages 1–9, 2013. 2

[86] Abdeslam Boularias, Jens Kober, and Jan Peters. Relative entropy inverse reinforcement learning. In *AISTATS*, pages 182–189, 2011. 3

[87] Navid Aghasadeghi and Timothy Bretl. Maximum entropy inverse reinforcement learning in continuous state spaces with path integrals. In *Intelligent Robots and Systems (IROS), 2011 IEEE/RSJ International Conference on*, pages 1561–1566. IEEE, 2011. 3

[88] Animesh Garg Daniel Crankshaw Joseph E. Gonzalez Ken Goldberg Richard Liaw, Sanjay Krishnan. Composing meta-policies for autonomous driving using hierarchical deep reinforcement learning. In *Robotics and Automation (ICRA), 2017 IEEE International Conference on*. IEEE, 2017.

[89] Jacob Andreas, Dan Klein, and Sergey Levine. Modular multitask reinforcement learning with policy sketches. *CoRR*, abs/1611.01796, 2016. URL `http://arxiv.org/abs/1611.01796`.

[90] Sascha Lange, Martin Riedmiller, and Arne Voigtlander. Autonomous reinforcement learning on raw visual input data in a real world application. In *Neural Networks (IJCNN), The 2012 International Joint Conference on*, pages 1–8. IEEE, 2012.

[91] Max Jaderberg, Volodymyr Mnih, Wojciech Marian Czarnecki, Tom Schaul, Joel Z. Leibo, David Silver, and Koray Kavukcuoglu. Reinforcement learning with unsupervised auxiliary tasks. *CoRR*, abs/1611.05397, 2016. URL `http://arxiv.org/abs/1611.05397`.

[92] Chelsea Finn, Xin Yu Tan, Yan Duan, Trevor Darrell, Sergey Levine, and Pieter Abbeel. Deep spatial autoencoders for visuomotor learning. In *Robotics and Automation (ICRA), 2016 IEEE International Conference on*, pages 512–519. IEEE, 2016.

[93] Manuel Watter, Jost Springenberg, Joschka Boedecker, and Martin Riedmiller. Embed to control: A locally linear latent dynamics model for control from raw images. In *Advances in Neural Information Processing Systems*, pages 2746–2754, 2015.

[94] Walther Wachenfeld, Hermann Winner, J Chris Gerdes, Barbara Lenz, Markus Maurer, Sven Beiker, Eva Fraedrich, and Thomas Winkle. Use cases for autonomous driving. In *Autonomous Driving*, pages 9–37. Springer, 2016.

[95] Yarin Gal and Zoubin Ghahramani. Dropout as a bayesian approximation: Representing model uncertainty in deep learning. *arXiv preprint arXiv:1506.02142*, 2015.

[96] Marco Pavone. Autonomous mobility-on-demand systems for future urban mobility. In *Autonomous Driving*, pages 387–404. Springer, 2016.

[97] Tomasz Janasz and Uwe Schneidewind. The future of automobility. In *Shaping the Digital Enterprise*, pages 253–285. Springer, 2017.

[98] William J Mitchell, Chris E Borroni-Bird, and Lawrence D Burns. *Reinventing the automobile: Personal urban mobility for the 21st century*. 2010.

[99] Kevin Spieser, Kyle Treleaven, Rick Zhang, Emilio Frazzoli, Daniel Morton, and Marco Pavone. Toward a systematic approach to the design and evaluation of automated mobility-on-demand systems: A case study in singapore. In *Road Vehicle Automation*, pages 229–245. Springer, 2014.

[100] Ryan Kiros, Ruslan Salakhutdinov, and Richard S Zemel. Multimodal neural language models. In *international Conference on Machine Learning (ICML)*, volume 14, pages 595–603, 2014.

[101] Nitish Srivastava and Ruslan R Salakhutdinov. Multimodal learning with deep boltzmann machines. In *Advances in neural information processing systems*, pages 2222–2230, 2012.

[102] Jiquan Ngiam, Aditya Khosla, Mingyu Kim, Juhan Nam, Honglak Lee, and Andrew Y Ng. Multimodal deep learning. In *Proceedings of the 28th international conference on machine learning (ICML-11)*, pages 689–696, 2011.

[103] Alex Graves, Abdel-rahman Mohamed, and Geoffrey Hinton. Speech recognition with deep recurrent neural networks. In *Acoustics, speech and signal processing (icassp), 2013 ieee international conference on*, pages 6645–6649. IEEE, 2013.

[104] Brandon Amos, Lei Xu, and J. Zico Kolter. Input convex neural networks. *arXiv preprint arXiv:1609.07152*, 2016.

[105] Geoffrey Hinton, Li Deng, Dong Yu, George E Dahl, Abdel-rahman Mohamed, Navdeep Jaitly, Andrew Senior, Vincent Vanhoucke, Patrick Nguyen, Tara N Sainath, et al. Deep neural networks for acoustic modeling in speech recognition: The shared views of four research groups. *IEEE Signal Processing Magazine*, 29(6):82–97, 2012.

[106] Karen Simonyan and Andrew Zisserman. Very deep convolutional networks for large-scale image recognition. In *International Conference on Learning Representations (ICLR)*, 2015.

[107] Alex Krizhevsky, Ilya Sutskever, and Geoffrey E Hinton. Imagenet classification with deep convolutional neural networks. In *Advances in neural information processing systems*, pages 1097–1105, 2012.

[108] Jacob Andreas, Marcus Rohrbach, Trevor Darrell, and Dan Klein. Deep compositional question answering with neural module networks. *CoRR*, abs/1511.02799, 2015. URL `http://arxiv.org/abs/1511.02799`.

[109] Andrei A Rusu, Matej Vecerik, Thomas Rothörl, Nicolas Heess, Razvan Pascanu, and Raia Hadsell. Sim-to-real robot learning from pixels with progressive nets. *arXiv preprint arXiv:1610.04286*, 2016.

[110] Greg Brockman, Vicki Cheung, Ludwig Pettersson, Jonas Schneider, John Schulman, Jie Tang, and Wojciech Zaremba. Openai gym. *arXiv preprint arXiv:1606.01540*, 2016.

[111] Richard S Sutton and Andrew G Barto. *Reinforcement learning: An introduction*, volume 1. MIT press Cambridge, 1998.

[112] Greg Brockman, Vicki Cheung, Ludwig Pettersson, Jonas Schneider, John Schulman, Jie Tang, and Wojciech Zaremba. Openai gym, 2016.

[113] Matthias Plappert. keras-rl. `https://github.com/matthiasplappert/keras-rl`, 2016.

[114] Fereshteh Sadeghi and Sergey Levine. (cad)2rl: Real single-image flight without a single real image. *arXiv preprint arXiv:1611.04201*, 2016.

[115] Nicolas Heess, Jonathan J Hunt, Timothy P Lillicrap, and David Silver. Memory-based control with recurrent neural networks. *arXiv preprint arXiv:1512.04455*, 2015.

[116] Greg Brockman, Vicki Cheung, Ludwig Pettersson, Jonas Schneider, John Schulman, Jie Tang, and Wojciech Zaremba. Openai gym. *arXiv preprint arXiv:1606.01540*, 2016.

[117] Martín Abadi, Ashish Agarwal, Paul Barham, Eugene Brevdo, Zhifeng Chen, Craig Citro, Greg S Corrado, Andy Davis, Jeffrey Dean, Matthieu Devin, et al. Tensorflow: Large-scale machine learning on heterogeneous distributed systems. *arXiv preprint arXiv:1603.04467*, 2016.

[118] François Chollet. Keras (2015). *URL http://keras. io*.

[119] P. Langley. Crafting papers on machine learning. In Pat Langley, editor, *Proceedings of the 17th International Conference on Machine Learning (ICML 2000)*, pages 1207–1216, Stanford, CA, 2000. Morgan Kaufmann.

[120] Eder Santana and George Hotz. Learning a driving simulator. *arXiv preprint arXiv:1608.01230*, 2016.

[121] Steven Bohez, Tim Verbelen, Elias De Coninck, Bert Vankeirsbilck, Pieter Simoens, and Bart Dhoedt. Sensor fusion for robot control through deep reinforcement learning. *arXiv preprint arXiv:1703.04550*, 2017.

[122] Gustav Larsson, Michael Maire, and Gregory Shakhnarovich. Fractalnet: Ultra-deep neural networks without residuals. *arXiv preprint arXiv:1605.07648*, 2016.

[123] Allen Nie. Stochastic dropout: Activation-level dropout to learn better neural language models.

[124] Yarin Gal and Zoubin Ghahramani. Dropout as a bayesian approximation: Representing model uncertainty in deep learning. *arXiv preprint arXiv:1506.02142*, 2, 2015.

[125] James Andrew Bagnell, David Bradley, David Silver, Boris Sofman, and Anthony Stentz. Learning for autonomous navigation. *IEEE Robotics & Automation Magazine*, 17(2): 74–84, 2010.

[126] Keonyup Chu, Minchae Lee, and Myoungho Sunwoo. Local path planning for off-road autonomous driving with avoidance of static obstacles. *IEEE Transactions on Intelligent Transportation Systems*, 13(4):1599–1616, 2012.

[127] Genya Ishigami, Keiji Nagatani, and Kazuya Yoshida. Path planning and evaluation for planetary rovers based on dynamic mobility index. In *Intelligent Robots and Systems (IROS), 2011 IEEE/RSJ International Conference on*, pages 601–606. IEEE, 2011.

[128] Mark Cutler and Jonathan P How. Efficient reinforcement learning for robots using informative simulated priors. In *Robotics and Automation (ICRA), 2015 IEEE International Conference on*, pages 2605–2612. IEEE, 2015.

[129] Dave Ferguson and Anthony Stentz. Field d*: An interpolation-based path planner and replanner. In *Robotics research*, pages 239–253. Springer, 2007.

[130] Sven Koenig and Maxim Likhachev. Improved fast replanning for robot navigation in unknown terrain. In *Robotics and Automation, 2002. Proceedings. ICRA'02. IEEE International Conference on*, volume 1, pages 968–975. IEEE, 2002.

[131] Aviv Tamar, Yi Wu, Garrett Thomas, Sergey Levine, and Pieter Abbeel. Value iteration networks. In *Advances in Neural Information Processing Systems*, pages 2154–2162, 2016.

[132] David Stavens and Sebastian Thrun. A self-supervised terrain roughness estimator for off-road autonomous driving. *arXiv preprint arXiv:1206.6872*, 2012.

[133] Panagiotis Papadakis. Terrain traversability analysis methods for unmanned ground vehicles: A survey. *Engineering Applications of Artificial Intelligence*, 26(4):1373–1385, 2013.

[134] Sergey Levine, Zoran Popovic, and Vladlen Koltun. Nonlinear inverse reinforcement learning with gaussian processes. In *Advances in Neural Information Processing Systems*, pages 19–27, 2011.

[135] Edouard Klein, Matthieu Geist, Bilal Piot, and Olivier Pietquin. Inverse reinforcement learning through structured classification. In *Advances in Neural Information Processing Systems*, pages 1007–1015, 2012.

[136] Kyungjae Lee, Sungjoon Choi, and Songhwai Oh. Inverse reinforcement learning with leveraged gaussian processes. In *Intelligent Robots and Systems (IROS), 2016 IEEE/RSJ International Conference on*, pages 3907–3912. IEEE, 2016.

[137] Brian D Ziebart, Nathan Ratliff, Garratt Gallagher, Christoph Mertz, Kevin Peterson, J Andrew Bagnell, Martial Hebert, Anind K Dey, and Siddhartha Srinivasa. Planning-based prediction for pedestrians. In *Intelligent Robots and Systems, 2009. IROS 2009. IEEE/RSJ International Conference on*, pages 3931–3936. IEEE, 2009.